博士論文（要約）

Study of novel superconducting states in tetragonal phase of Fe(Se,S) by laser-based angle-resolved photoemission spectroscopy

(レーザー角度分解光電子分光による 正方晶相Fe(Se,S)における超伝導状態の研究)

長島　椿

Contents

Introduction

Since the discovery of superconductivity by Onnes in 1911, even though more than one century has gone by, the detailed mechanism of this macroscopic quantum phenomenon has been unresolved mainly because of the existence of unconventional superconductors which can not be explained by the phonon-mediated paring mechanism proposed in the BCS theory. Unconventional superconductors are expected as a platform of a variety of intriguing states and to pave the way for understanding the mechanism of superconductivity. On the other hand, typically they have low critical temperature T_{c} and require cryogenic systems to keep the states, which makes it difficult to realize industrial applications and approach experimentally.

Angle-resolved photoemission spectroscopy (ARPES) is a unique and powerful tool to investigate electronic structures by direct observations of electrons in momentum space. Electrons in solids are emitted by excitation caused by incident light whose energy is higher than the work function specific to the material, which tells binding energy and momentum of electrons represented via kinetic energy and emission angle respectively. Generally the relation between energy resolution and efficiency of measurements is trade-off and this had restricted further improvement of resolution in ARPES and prevented from study for some unconventional superconductors with low T_{c}. As a solution for this problem, we developed and installed a new deep ultraviolet high intensity continuous wave laser light source for high resolution ARPES measurements.

As a target for measurements, we focused on a substitutional system of $\mathrm{FeSe}_{1-x}\mathrm{S}_x$ that is an unique system among iron-based superconductors for that it has nematic quantum criticality without magnetic ordering. It is expected that the superconducting state in the tetragonal phase differs from that in the nematic phase, and especially the former is suggested to be the ultranodal states with a Bogoliubov Fermi surface (BFS).

This thesis is composed as follows. In Chapter 1, the basis of superconductivity is explained and also it introduces unconventional superconductors. In Chapter 2, the principle of ARPES is described and Chapter 3 introduces the laser-based ARPES (laser ARPES) system used in this thesis. Chapter 4 gives explanations about the installation and improvements of the new developed laser light source to attain high resolution. We then go on Chapter 5 to present the superconducting state in the tetragonal phase of Fe(Se,S). It was found that the gap anisotropy has 2-fold rotational symmetry showing nodes in the finite areas in momentum space which refers to BFS

in the ultranodal state. Finally Chapter 6 concludes this thesis.

Chapter 1

Superconductivity

From the discovery of superconductivity from Hg cooled with liquid He by Onnes in 1911, this macroscopic quantum phenomenon has been expected and studied for a variety of applications for superconducting wires of zero resistivity, superconducting magnets et cetera, though it is prevented from the realization owing to the quite low critical temperature $T_{\rm c}$. Superconductors can be generally categorized into the conventional ones, which can be explained by the BCS theory, and the others, the unconventional ones. Among the formers, $T_{\rm c}$ is comparatively low and its maximum is limited according to the theory. On the other hand, the latter includes high $T_{\rm c}$ superconductors such as cuprate superconductors and iron-based superconductors, and attracts interest in terms of further enhancement of $T_{\rm c}$. In this context, it plays the significant role to deepen the understanding of the mechanism behind these superconductors. This chapter explains the BCS theory and theoretical insights for unconventional superconductivity.

1.1 BCS theory

The BCS theory developed by Bardeen, Cooper and Shrieffer in 1957 describes the microscopic view of superconducting states realized with electron pairs called Cooper pairs that is formed through attractive interaction. This section gives explanations of the BCS theory[1, 2].

Let us assume the pair formation around the Fermi surface (FS) by an attraction between electrons via phonon, and also suppose it is spin-singlet pairing whose angular momentum is zero. Then, interactions between electrons can be written with a matrix element $V(\boldsymbol{k}', \boldsymbol{k})$ as

$$\begin{aligned}\mathcal{H}_{int} &= \frac{1}{2}\sum_{\boldsymbol{k}\boldsymbol{k}'} V(\boldsymbol{k}', \boldsymbol{k})(c^\dagger_{-\boldsymbol{k}'\downarrow} c^\dagger_{\boldsymbol{k}'\uparrow} c_{\boldsymbol{k}\uparrow} c_{-\boldsymbol{k}\downarrow} + c^\dagger_{-\boldsymbol{k}'\uparrow} c^\dagger_{\boldsymbol{k}'\downarrow} c_{\boldsymbol{k}\downarrow} c_{-\boldsymbol{k}\uparrow}) \\ &= \sum_{\boldsymbol{k}\boldsymbol{k}'} V(\boldsymbol{k}', \boldsymbol{k}) c^\dagger_{-\boldsymbol{k}'\downarrow} c^\dagger_{\boldsymbol{k}'\uparrow} c_{\boldsymbol{k}\uparrow} c_{-\boldsymbol{k}\downarrow}. \end{aligned} \tag{1.1}$$

Adding kinetic energy of electrons and applying mean-field approximation, the Hamiltonian is represented as follows

$$\mathcal{H} = \sum_{\boldsymbol{k}\sigma} \xi_{\boldsymbol{k}} c^{\dagger}_{\boldsymbol{k}\sigma} c_{\boldsymbol{k}\sigma} - \sum_{\boldsymbol{k}} (\Delta_{\boldsymbol{k}} c^{\dagger}_{-\boldsymbol{k}\downarrow} c^{\dagger}_{\boldsymbol{k}\uparrow} + \text{h.c.}) + \sum_{\boldsymbol{k}} \Delta_{\boldsymbol{k}} \langle c^{\dagger}_{-\boldsymbol{k}\downarrow} c^{\dagger}_{\boldsymbol{k}\uparrow} \rangle. \tag{1.2}$$

where $\xi_{\boldsymbol{k}} = \epsilon_{\boldsymbol{k}} - \mu$ is the energy of electrons with respect to the chemical potential μ, and $\Delta_{\boldsymbol{k}}$ is the gap function given as

$$\Delta_{\boldsymbol{k}} = -\sum_{\boldsymbol{k}'} V(\boldsymbol{k}', \boldsymbol{k}) \langle c_{\boldsymbol{k}'\uparrow} c_{-\boldsymbol{k}'\downarrow} \rangle, \tag{1.3}$$

To diagonalize this Hamiltonian, the Bogoliubov transformation is applied, that is,

$$\begin{aligned} \alpha_{\boldsymbol{k}\uparrow} &= u_{\boldsymbol{k}} c_{\boldsymbol{k}\uparrow} - v_{\boldsymbol{k}} c^{\dagger}_{-\boldsymbol{k}\downarrow} \\ \alpha^{\dagger}_{-\boldsymbol{k}\downarrow} &= u_{\boldsymbol{k}} c^{\dagger}_{-\boldsymbol{k}\downarrow} + v^{*}_{\boldsymbol{k}} c_{\boldsymbol{k}\uparrow}. \end{aligned} \tag{1.4}$$

These annihilation and creation operators $\alpha_{\boldsymbol{k}\uparrow}$ and $\alpha^{\dagger}_{-\boldsymbol{k}\downarrow}$ of the fermionic quasiparticles requires $\{\alpha_{\boldsymbol{k}\uparrow},\, \alpha^{\dagger}_{\boldsymbol{k}\uparrow}\} = 1$ due to the Pauli principle. Then, the coefficients in the last equations have to satisfy the following condition,

$$u^2_{\boldsymbol{k}} + |v_{\boldsymbol{k}}|^2 = 1. \tag{1.5}$$

With its inverse transformation,

$$\begin{aligned} c_{\boldsymbol{k}\uparrow} &= u_{\boldsymbol{k}} \alpha_{\boldsymbol{k}\uparrow} + v_{\boldsymbol{k}} \alpha^{\dagger}_{-\boldsymbol{k}\downarrow} \\ c^{\dagger}_{-\boldsymbol{k}\downarrow} &= u_{\boldsymbol{k}} \alpha^{\dagger}_{-\boldsymbol{k}\downarrow} - v^{*}_{\boldsymbol{k}} \alpha_{\boldsymbol{k}\uparrow}, \end{aligned} \tag{1.6}$$

(1.2) is diagonalized making the coefficients $\alpha_{-\boldsymbol{k}\downarrow}\alpha_{\boldsymbol{k}\uparrow}$ and $\alpha^{\dagger}_{\boldsymbol{k}\uparrow}\alpha^{\dagger}_{-\boldsymbol{k}\downarrow}$ zeros, which imposes

$$2\xi_{\boldsymbol{k}} u_{\boldsymbol{k}} v^{*}_{\boldsymbol{k}} - \Delta_{\boldsymbol{k}} |v_{\boldsymbol{k}}|^2 + \Delta^{*}_{\boldsymbol{k}} u^2_{\boldsymbol{k}} = 0. \tag{1.7}$$

From (1.5) and (1.7), we can deduce the relations below,

$$u^2_{\boldsymbol{k}} = \frac{1}{2}\left(1 + \frac{\xi_{\boldsymbol{k}}}{E_{\boldsymbol{k}}}\right),\ |v_k|^2 = \frac{1}{2}\left(1 - \frac{\xi_{\boldsymbol{k}}}{E_{\boldsymbol{k}}}\right) \tag{1.8}$$

$$E_k = \sqrt{\xi^2_{\boldsymbol{k}} + |\Delta_{\boldsymbol{k}}|^2}. \tag{1.9}$$

Thus, the Hamiltonian becomes

$$
\begin{aligned}
\mathcal{H} &= \sum_k [(u_k^2 \alpha_{k\uparrow}^\dagger \alpha_{k\uparrow} + |v_k|^2 \alpha_{-k\downarrow} \alpha_{-k\downarrow}^\dagger) + (u_k^2 \alpha_{-k\downarrow}^\dagger \alpha_{-k\downarrow} + |v_k|^2 \alpha_{k\uparrow} \alpha_{k\uparrow}^\dagger)] \\
&- \sum_k [\Delta_k (u_k v_k^* \alpha_{-k\downarrow}^\dagger \alpha_{-k\downarrow} - v_k^* u_k \alpha_{k\uparrow} \alpha_{k\uparrow}^\dagger) + \Delta_k^* (-u_k v_k \alpha_{k\uparrow} \alpha_{k\uparrow}^\dagger + v_k u_k \alpha_{-k\downarrow}^\dagger \alpha_{-k\downarrow})] \\
&+ \sum_k \Delta_k \langle c\,\dagger_{-k\downarrow}\, \alpha_{k\uparrow}^\dagger \rangle \\
&= \sum_k [2\xi_k |v_k|^2 + \xi_k (u_k^2 - |v_k|^2)(\alpha_{k\uparrow}^\dagger \alpha_{k\uparrow} + \alpha_{-k\downarrow}^\dagger \alpha_{-k\downarrow})] \\
&- \sum_k [-(\Delta_k u_k v_k^* + \Delta_k^* u_k v_k) + (\Delta_k u_k v_k^* + \Delta_k^* u_k v_k)(\alpha_{k\uparrow}^\dagger \alpha_{k\uparrow} + \alpha_{-k\downarrow}^\dagger \alpha_{-k\downarrow})] \\
&+ \sum_k \Delta_k \langle c_{-k\downarrow}^\dagger c_{k\uparrow}^\dagger \rangle. \qquad (1.10)
\end{aligned}
$$

Using the property $\alpha_{k\sigma}\alpha_{k\sigma}^\dagger = 1 - \alpha_{k\sigma}^\dagger \alpha_{k\sigma}$ for the first and second lines, we can finally find

$$
\mathcal{H} = E_g + \sum_k E_k (\alpha_{k\uparrow}^\dagger \alpha_{k\uparrow} + \alpha_{-k\downarrow}^\dagger \alpha_{-k\downarrow}). \qquad (1.11)
$$

$$
E_g = \sum_k (2\xi_k |v_k|^2 + 2\Delta_K u_k v_k^* + \Delta_k \langle c_{-k\downarrow}^\dagger c_{k\uparrow}^\dagger \rangle), \qquad (1.12)
$$

The notations of $\alpha_{\boldsymbol{k}\uparrow}^\dagger \alpha_{\boldsymbol{k}\uparrow}$ and $\alpha_{-\boldsymbol{k}\downarrow}^\dagger \alpha_{-\boldsymbol{k}\downarrow}$ in the second term in (1.11) represent the particle number operators of the Bogoliubov quasiparticles with spin up and down respectively, and then this Hamiltonian can be interpreted as a free fermion system of the quasiparticles with the excitation energy $E_{\boldsymbol{k}}$ in (1.9) from the ground state whose energy is given by (1.12).

1.2 Temperature dependence of the superconducting gap

The superconducting gap $\Delta_{\boldsymbol{k}}$ is closed as the temperature from $T = 0$. This means that breaking the Cooper pairs and creating two quasiparticles as the elementary excitation requires energy, which conclude a reduction of energy for the pair condensation, and shrinkage of $\Delta_{\boldsymbol{k}}$. This decrease generates the elementary excitations as thermal excitations, and eventually the size of $\Delta_{\boldsymbol{k}}$ radically diminishes. Here its temperature dependence is explained qualitatively.

The expectation value of the number of the particles is given by the Fermi distribution function $f(E_{\boldsymbol{k}})$

$$\langle \alpha_{-\boldsymbol{k}\downarrow}\alpha_{\boldsymbol{k}\uparrow}\rangle = \langle \alpha^{\dagger}_{\boldsymbol{k}\uparrow}\alpha^{\dagger}_{-\boldsymbol{k}\downarrow}\rangle = f(E_{\boldsymbol{k}}). \tag{1.13}$$

Here, the transformation in (1.4) is applied, which leads to

$$\langle c_{\boldsymbol{k}\uparrow}c_{-\boldsymbol{k}\downarrow}\rangle = \frac{\Delta_{\boldsymbol{k}}}{2E_{\boldsymbol{k}}}\tanh\frac{1}{2}\beta E_{\boldsymbol{k}}. \tag{1.14}$$

The equation for the energy of quasiparticles in (1.9) becomes $|\Delta_{\boldsymbol{k}}|$ at the Fermi level, and turn with the equations (1.3) and (1.14) into

$$\Delta_{\boldsymbol{k}} = -\sum_{\boldsymbol{k}'} V(\boldsymbol{k}', \boldsymbol{k})\frac{\Delta_{\boldsymbol{k}'}}{2E_{\boldsymbol{k}'}}\tanh\frac{1}{2}\beta E_{\boldsymbol{k}'}, \tag{1.15}$$

which is called a gap equation. Assuming an attraction -V works within $\hbar\omega_D$ from the Fermi level, and $\Delta_{\boldsymbol{k}}$ is a momentum-independent constant Δ_0,we obtain

$$1 \simeq VN(\epsilon_F)\log\frac{2\hbar\omega_D}{\Delta_0}. \tag{1.16}$$

When $T \to 0$K, the gap size becomes

$$\Delta_0 = 2\hbar\omega_D e^{-\frac{1}{VN(\epsilon_F)}}. \tag{1.17}$$

We can determine T_{c} as the critical temperature from the superconducting state to the normal state supposing $\Delta_0 \to 0$, then

$$k_{\mathrm{B}}T_{\mathrm{c}} = 1.13\hbar\omega_D e^{-\frac{1}{VN(\epsilon_F)}} \tag{1.18}$$

is obtained. Therefore, considering Eq. (1.17) and (1.18), the ratio of them is

$$\frac{2\Delta_0}{k_{\mathrm{B}}T_{\mathrm{c}}} = 3.53, \tag{1.19}$$

which is the universal constant for materials obeying to the BCS theory, and has been used as one of criteria to determine whether the superconductivity is the conventional or unconventional one.

1.3 Quasiparticle density of states

In studies of superconductivity, the quasiparticle density of states is one of significant physical quantities which is represented as

$$N(E) = \sum_{\boldsymbol{k}} \delta(E - E_{\boldsymbol{K}}). \tag{1.20}$$

Describing the density of states in the normal state as $N(\epsilon_F)$, the summation about E is

$$\sum_{\boldsymbol{k}} = N(\epsilon_F) \int dE, \tag{1.21}$$

so Eq. (1.20) is transformed into

$$N(E) = N(\epsilon_F) \int dE Re \frac{E}{\sqrt{E^2 - \Delta_{\boldsymbol{k}}^2}}. \tag{1.22}$$

In the BCS theory, the superconducting gap is constant putting $\Delta_{\boldsymbol{k}} = \Delta$, and $N(\epsilon_F)$ can also be treated as a constant because Δ is generally quite small with respect to the Fermi energy.

Thus, the quasiparticle density of states normalized by $N(\epsilon_F)$ is written as follows,

$$\begin{aligned} \frac{N(E)}{N(\epsilon_F)} &= Re \frac{E}{\sqrt{E^2 - \Delta_{\boldsymbol{k}}^2}} \\ &= \begin{cases} Re \dfrac{E}{\sqrt{E^2 - \Delta_{\boldsymbol{k}}^2}} \,\mathrm{if}(|\Delta| < E) \\ 0 \,\mathrm{if}(0 \leq E < |\Delta|). \end{cases} \end{aligned} \tag{1.23}$$

This equation gives insights to understand that for BCS superconductors, the states where $|E| < |\Delta|$ are excluded into the range where $|E| > |\Delta|$ to make the gap by 2Δ, and that the density of states diverges to infinity where $E \to \pm|\Delta|$.

1.4 Anisotropic superconductivity

The BCS theory shown above gives the explanation of isotropic superconductivity, of which superconducting gap is isotropic and does not depend on momentum. In these superconductors, electrons in a Cooper pair have spins of the opposite directions to each other, and its wave function contains a spin part which is asymmetric to exchange of two electrons. From this property and analogy to the classification of the atomic orbitals, conventional superconductors explained in the BCS theory are also called as isotropic s-wave superconductors.

On the other hand, there has been found unconventional superconductors which have the gap depending on momentum, commencing with d-wave superconductivity in cuprate superconductors [3], and they are known as anisotropic superconductors for the k-dependent superconducting gap. As distinct from conventional ones, anisotropic superconductors have different symmetries and correspondingly a variety of superconducting gap shapes. Theoretical studies have discussed the superconductivity symmetric to a spin exchange and known as triplet superconductivity such as p-wave and

f-wave. In terms of experiments, its realization has been suggested in some materials for instance UPt_3 [4] and Sr_2RuO_4 [5]. To understand the basis of the superconductivity not explained by the BCS theory, it is thought meaningful to research on the attractive interaction between Cooper pairs in respect of their symmetries.

1.4.1 Superconducting gap symmetry and density of states

The criteria for determination of the superconducting gap symmetry are whether nodes where the gap size becomes zero in momentum space and its k dependence. The isotropic s-wave conductivity has no node in the gap structure, besides there can be nodes at points or along lines, which are called as point nodes and line nodes, respectively. These characters are shown in the density of states, hence can be identified from the temperature dependence of specific heat C, spin-lattice relaxation rate $1/T_1$, and penetration depth λ. Tab. 1.1 shows the relations between superconducting gap structures and temperature dependence of physical quantities.

Table 1.1: Determination of the superconducting gap symmetry from temperature dependence. Temperature dependence of the density of states is reflected to one of each physical quantity, which enables distinguishment of the symmetry.

gap structure	C	$1/T_1$	λ
isotropic s-wave	$\exp(-\Delta/k_{\mathrm{B}}T_{\mathrm{c}})$		
line nodes	T^2	T^3	T^1
point nodes	T^3	T^5	T^2

All of these quantities depend on temperature exponentially in the case of the s-wave isotropic superconductivity, whereas they show different types of power law relations, respectively when points and line nodes exist.

1.4.2 Inversion symmetry breaking superconductors

In the system where an inverse crystal structure does not overlap the original structure, that is breaking the spatial inversion symmetry, the electric field gradient arises causing the antisymmetric spin-orbit coupling, and eventually makes the electronic bands split. Concerning superconductors, difference of the density of states between split Fermi surfaces enable to realize spin-singlet and triplet mixing states [6]. Here this phenomenon is explained from the point of view of symmetries [7].

The wave function of Cooper pairs is written as follows

$$\Delta(\boldsymbol{r}_1 - \boldsymbol{r}_2; s_1, s_2) = \Phi(\boldsymbol{r}_1 - \boldsymbol{r}_2)F(s_1, s_2) \tag{1.24}$$

where $\boldsymbol{r}$ and s represent the position of electron and spin, respectively. Suffix is given

for identification of electrons forming a Cooper pair. In addition, Φ and F represent the orbit and spin part in each. They are classified with parity as follows,

$$\begin{cases} \Phi_{\mathrm{even}}(-(\boldsymbol{r}_1 - \boldsymbol{r}_2)) = \Phi_{\mathrm{even}}(\boldsymbol{r}_1 - \boldsymbol{r}_2) \\ \Phi_{\mathrm{odd}}(-(\boldsymbol{r}_1 - \boldsymbol{r}_2)) = -\Phi_{\mathrm{odd}}(\boldsymbol{r}_1 - \boldsymbol{r}_2) \end{cases} \tag{1.25}$$

$$\begin{cases} F_s(s_2, s_1) = -F_s(s_1, s_2) \\ F_t(s_2, s_1) = F_s(s_1, s_2) \end{cases} \tag{1.26}$$

The sign does not change for even orbitals, but turns to the opposite for odd orbitals with respect to coordinate inversion. Also, antiparallel spins of spin-singlet states alter the sign and parallel spins of spin-triplet states keeps the original sign. On the other hand, the sign of the wave function of a Cooper pair has to be changed by exchanging particles due to the Pauli exclusion principle, that imposes the condition below,

$$\Delta(\boldsymbol{r}_1 - \boldsymbol{r}_2; s_1, s_2) = -\Delta(\boldsymbol{r}_2 - \boldsymbol{r}_1; s_2, s_1). \tag{1.27}$$

The sets of orbitals and spins satisfying Eq. (1.27), are allowed only to be

$$\Delta_{\mathrm{even},s}(\boldsymbol{r}_1 - \boldsymbol{r}_2; s_1, s_2) = \Phi_{\mathrm{even}}(\boldsymbol{r}_1 - \boldsymbol{r}_2) F_s(s_1, s_2) \tag{1.28}$$

$$\Delta_{\mathrm{odd},t}(\boldsymbol{r}_1 - \boldsymbol{r}_2; s_1, s_2) = \Phi_{\mathrm{odd}}(\boldsymbol{r}_1 - \boldsymbol{r}_2) F_t(s_1, s_2), \tag{1.29}$$

which are even orbital spin-singlet states and odd orbital spin-triplet states, respectively.

When the inversion symmetry is protected, the wave function is an eigenfunction of the parity operator $\hat{P}$ which gives coordinate inversion, then

$$\hat{P}\Delta = \pm\Delta. \tag{1.30}$$

$\hat{P}$ acts only to orbital parts as $\hat{P}\Phi_{\mathrm{even}} = \Phi_{\mathrm{even}}$ and $\hat{P}\Phi_{\mathrm{odd}} = -\Phi_{\mathrm{odd}}$. Considering the liner combination of two types of sets allowed above

$$\Delta = \Delta_{\mathrm{even},s} + c\Delta_{\mathrm{odd},t}\,(c = const.), \tag{1.31}$$

the following is obtained

$$\begin{aligned} \hat{P}\Delta &= \hat{P}\Delta_{\mathrm{even},s} + c\hat{P}\Delta_{\mathrm{odd},t} && (1.32) \\ &= \Delta_{\mathrm{even},s} - c\Delta_{\mathrm{odd},t} && (1.33) \\ &\neq \Delta, && (1.34) \end{aligned}$$

which no longer means an eigenstates leading a contradiction.

As shown in the foregoing, spin-singlet and triplet mixing states can not be realized in the inversion-symmetric systems. Thus, inversion symmetry breaking is required in order to keep the possibility to attain such mixing states. Moreover, for actual realization, it is necessary to develop different density of states between two split Fermi surfaces [8].

1.4.3 Time reversal symmetry broken superconductors

In unconventional superconductors, some materials are known as time-reversal symmetry broken superconductors such as UPt_3, Sr_2RuO_4 ,$LaNiC_2$, $LaNiGa_2$, Re-based superconductors, etc. [9–13].

Under time reversal operation, all momenta get reversal sign including contributions from spin angler momenta, and thus the TRS operator $\mathcal{T}$ works as

$$\mathcal{T}c^{\dagger}_{\boldsymbol{k}\uparrow} = -c_{-\boldsymbol{k}\downarrow}; \quad \mathcal{T}c^{\dagger}_{\boldsymbol{k}\downarrow} = c_{-\boldsymbol{k}\uparrow}, \tag{1.35}$$

which follows prohibition of a net magnetization in systems with TRS [14]. Therefore, an external field or spontaneous magnetization breaks TRS, and especially observation of the latter is evidence to detect the spontaneous TRSB, which is capable in muSR, optical Kerr effect, and superconducting quantum interference device (SQUID) magnetometry.

1.4.4 Novel superconducting states with additional degrees of freedom

Recently, new types of paring states have been proposed mainly in systems with additional degrees of freedom, for instance in multiband or multiorbital systems [15, 16]. Time is another candidate of new degrees of freedom which also can realize new parings conditions[17]. These features allow arrangements on the discussions based on the Pauli exclusion principle, for the sign change by particle exchange, which depends not only on orbitals and spin but also on new degrees of freedom in such systems.

Basically what we treat in experimental studies refers to the amplitude of the superconducting gap, and thus it is generally difficult to identify and approach to such paring states. However, it is suggested to realize a variety of novel superconducting states such as Bogoliubov Fermi surface, odd-frequency superconductivity, and anapole superconductivity with no-field FFLO states [18–21], and therefore further progress is expected in this area.

Chapter 2

Photoemission spectroscopy

Electrons are emitted from inside of solids by excitations derived from irradiation of light with higher energy than the work function of the material, and called photoelectrons. Applying this effect, namely external photoelectric effect, we can obtain the information about electronic structures of solids as a function of energy, which is photoelectron spectroscopy and used in this study. This chapter explains details and our setup of the experimental method [22–25].

2.1 Principle of photoemission spectroscopy

The time scale required for electronic transitions is generally expected as $10^{-15\text{-}16}$ seconds and much smaller than one of nuclear vibrations that is $10^{-12\text{-}14}$ seconds, This enable a discussion on the electric transitions ignoring effects from relaxation due to lattice vibrations, which is called the Franck-Condon principle. Excited electrons are also affected from scattering by collisions to other electrons before emission, that is to say electron correlation. Here, however, let us ignore each electron correlations supposing the one-electron approximation where photoelectrons moves independently under potentials from other electrons. In addition, we will treat three-step-model which describes the photoemission process dividing into three:

i. An electron at the energy level apart by the binding energy E_B from the Fermi level E_F got excited above the vacuum level E_{vac} by incident light with energy $\hbar\nu$ which is more than the work function Φ.

ii. An excited electron moves to the solid surface.

iii. A photoelectron is emitted from the solid surface.

After the emission, the photoelectron has the kinetic energy

$$E_{kin} = E_i - E_{vac} \tag{2.1}$$

and the energy conservation law imposes as follows,

$$\hbar\nu = E_f - E_i = E_{kin} + \phi + E_B \tag{2.2}$$

Figure 2.1 shows the relation of energy levels and photoelectron spectra in these process. If the energy of incident light and work function proper to substances are specified and substituted to the relation, we can obtain the binding energy inside of materials from the kinetic energy of photoelectrons in observed spectra whose intensity corresponds to the density of states and lets us approach to occupied states in solids. Under the one-electron approximation, the binding energy is considered to be equal to the energy of Bloch electron according to the Koopmans' theorem that is,

$$E_B = -\epsilon_{\boldsymbol{k}} \tag{2.3}$$

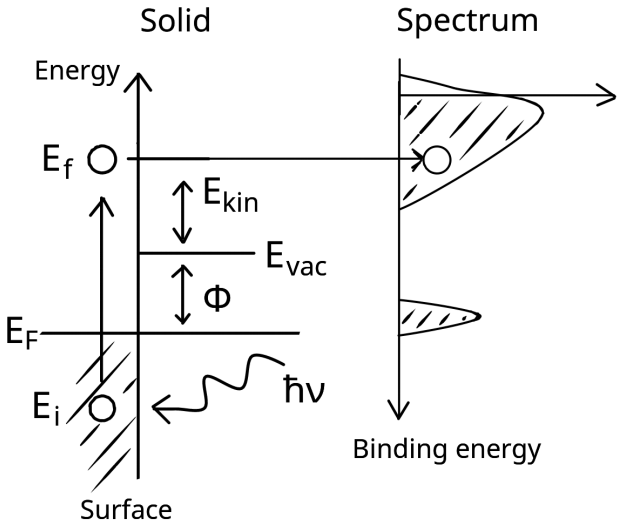

Figure 2.1: Relation between the energy levels and photoelectron spectra in the three-step-model. See the texts for details of parameters in the image.

Regarding photoemission process as an operation depriving an electron with energy ϵ in an N-electron system, it is written as follows,

$$E_B = -\epsilon + \mu \tag{2.4}$$
$$= E_i^{N-1} - E_g^N + \mu, \tag{2.5}$$

where E_i^{N-1} and E_g^N refer to the eigenvalue of the N-1-electron system and one of the ground state in the N-electron system Ψ_g^N, and μ is the chemical potential. Photoelectron spectra can be represented applying the Fermi's golden rule as

$$I(\boldsymbol{k},\epsilon) = \sum_{f,i} w_{i\to f} \tag{2.6}$$

$$\propto |\langle \Psi_i^{N-1}|c_{\boldsymbol{k}}|\Psi_g^N\rangle|^2 \delta(\epsilon + E_i^{N-1} - E_g^N). \tag{2.7}$$

Here, using the one-particle Green's function, let us describe the space and time evolution of an electron and a hole added to the electron system. A retarded Green's function is defined to be

$$G^{(R)}(\boldsymbol{k},t) \equiv -i\theta(t)\langle\{c_{\boldsymbol{k}}(t), c_{\boldsymbol{k}}^\dagger(0)\}\rangle, \tag{2.8}$$

where $\theta(t)$ is a step function and $c_{\boldsymbol{k}}(t)$ is for the Heisenberg representation. Then, from the Fourier transformation of $G^{(R)}(\boldsymbol{k},t)$, we obtains the followings

$$E_B = -i\int_0^\infty dt\langle\{c_{\boldsymbol{k}}(t), c_{\boldsymbol{k}}^\dagger(0)\}\rangle e^{i(\epsilon+i\delta)t} \tag{2.9}$$

$$= \sum_i |\langle \Psi_i^{N-1}|c_{\boldsymbol{k}}|\Psi_g^N\rangle|^2 (\frac{1}{\epsilon - E_i^{N+1} + E_g^N + i\delta} + \frac{1}{\epsilon + E_i^{N+1} - E_g^N + i\delta}, \tag{2.10}$$

whose first and second term represents adding an electron and a hole respectively. Moreover, using a relation about the principal integration $\mathcal{P}$ that is

$$\frac{1}{X+i\delta} = \mathcal{P}\frac{1}{X} - i\pi\delta(X), \tag{2.11}$$

the spectral function measured in PES becomes

$$A(\boldsymbol{k},\epsilon) = -\frac{1}{\pi} ImG^{(R)}(\boldsymbol{k},\epsilon) \tag{2.12}$$

$$= \sum_i |\langle \Psi_i^{N-1}|c_{\boldsymbol{k}}|\Psi_g^N\rangle|^2 \delta(\epsilon + E_i^{N+1} - E_g^N)\,(\epsilon < \mu), \tag{2.13}$$

which means the probability of the emission of an electron with energy ϵ and wavenumber $\boldsymbol{k}$. From equations (2.6) and(2.13), the correspondence between photoelectron spectra and spectrum function as shown below,

$$I(\boldsymbol{k},\epsilon) \propto A(\boldsymbol{k},\epsilon). \tag{2.14}$$

In the one-electron approximation, a substitution $E_i^{N-1} - E_g^N$ obtained by equations (2.3) and (2.4) for Eq. (2.13) leads

$$A(\boldsymbol{k},\epsilon) = \delta(\epsilon - \epsilon_{\boldsymbol{k}}), \tag{2.15}$$

which gives a sharp peak structure as a delta function in the spectral function. In a case with electron coupling, on the other hand, interacting quasiparticles arise instead of creation/annihilation of electrons and holes. The energy of quasiparticles deviates from $\epsilon = \epsilon_{\boldsymbol{k}}$, and there are finite energy width and lifetime $\tau_{\boldsymbol{k}}$. Defining the quasiparticle self-energy with the real part which corresponds to the energy deviation, and the imaginary part proportional to the energy width, the retarded Green's function can be written as the Dyson's equation below,

$$G^{(R)}(\boldsymbol{k}, \epsilon) = \frac{1}{\epsilon - \epsilon_{\boldsymbol{k}} - \Sigma(\boldsymbol{k}, \epsilon)}. \tag{2.16}$$

Considering this, the spectral function is revised to be

$$A(\boldsymbol{k}, \epsilon) = -\frac{1}{\pi} ImG^{(R)}(\boldsymbol{k}, \epsilon) \tag{2.17}$$

$$= -\frac{1}{\pi} \frac{Im\Sigma(\boldsymbol{k}, \epsilon)}{[\epsilon - \epsilon_{\boldsymbol{k}} - Re\Sigma(\boldsymbol{k}, \epsilon)]^2 + [Im\Sigma(\boldsymbol{k}, \epsilon)]^2}. \tag{2.18}$$

Therefore, the peak of $A(\boldsymbol{k}, \epsilon)$ is given from the equation $\epsilon = \epsilon_{\boldsymbol{k}} + Re\Sigma(\boldsymbol{k}, \epsilon)$ by its solution $\epsilon = \epsilon^*_{v_k}$, which describes the quasiparticle band as shown in Fig. (2.2). Applying the Taylor series to $Re\Sigma(\boldsymbol{k}, \epsilon)$ around $\epsilon = \epsilon^*_{v_k}$ and substituting it to Eq. (2.17), we obtain

$$A(\boldsymbol{k}, \epsilon) \simeq -\frac{z_{\boldsymbol{k}}(\epsilon^*_{\boldsymbol{k}})}{\pi} \frac{z_{\boldsymbol{k}}(\epsilon^*_{\boldsymbol{k}}) Im\Sigma(\boldsymbol{k}, \epsilon)}{[\epsilon = \epsilon^*_{v_k}]^2 + [z_{\boldsymbol{k}}(\epsilon^*_{\boldsymbol{k}}) Im\Sigma(\boldsymbol{k}, \epsilon)]} \tag{2.19}$$

$$z_{\boldsymbol{k}}(\epsilon) = [1 - \frac{\partial Re\Sigma(\boldsymbol{k}, \epsilon)}{\partial \epsilon}]^{-1}. \tag{2.20}$$

where Eq. (2.20) is called a renormalization factor. Eq. (2.17) indicates that the spectral function around the quasiparticle peak is approximated by the Lorentzian function whose integrated intensity is $z_{\boldsymbol{k}}(\epsilon^*_{\boldsymbol{k}}) < 1$ and FWHM is $-2z_{\boldsymbol{k}}(\epsilon^*_{\boldsymbol{k}}) Im\Sigma(\boldsymbol{k}, \epsilon^*_{\boldsymbol{k}})$.

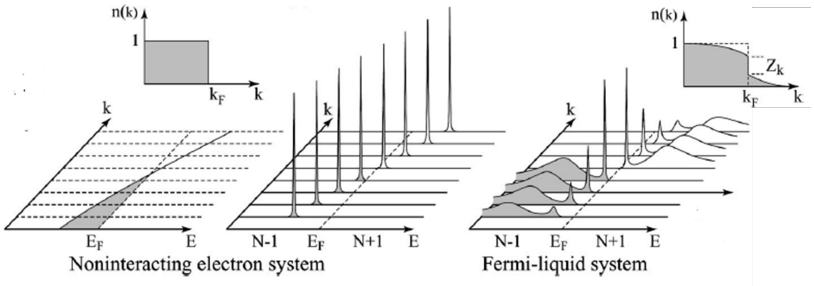

Figure 2.2: Change in the shapes of photoelectron spectra depending on whether electron coupling exists. In the case with electron coupling, broad and incoherent peaks appears other than quasiparticle peaks, and the wavenumber distribution decreases discontinuously by z_k at the Fermi level [24].

2.2 Angle-resolved photoemission spectroscopy

Angle-resolved photoemission spectroscopy gives information about electron momentum for it does not measure only kinetic energies of photoelectrons but also emission angles respect to the crystal surface, which enables observations of band dispersions and Fermi surfaces,, and its general configuration is shown in Fig. 2.3. Concerning momentum, the component parallel to the crystal surface $p_{\parallel}$ is conserved inside of solids and in vacuum because of the translational symmetry, besides the perpendicular component $p_{\perp}$ is changed. Considering a photoelectron emitted in vacuum as a free electron, its kinetic energy is $E_{kin} = \frac{\hbar^2 \boldsymbol{k}^2}{2m}$ and $p_{\perp}$ is

$$p_{\perp} = \hbar \boldsymbol{k}_{\perp} = \sqrt{2mE_{kin}} \cdot \sin\theta, \tag{2.21}$$

where θ is the polar angle of the photoemission. In actual experiments, θ can be so large that the measured range exceeds the first Brillouin zone, in which case a reciprocal lattice vector G is subtracted from $\boldsymbol{k}$, and this crystal momentum is substituted. $\mathrm{p}_{\perp}$ is given by

$$\mathrm{p}_{\perp} = \hbar \boldsymbol{k}_{\perp} = \sqrt{2m(E_{kin}\cos\theta^2 + V_0)}, \tag{2.22}$$

where V_0 is an inner potential. A wavenumber dispersion perpendicular to the crystal surface can be ignored for low-dimensional systems, and the band dispersion is determined only by $\boldsymbol{k}_{\parallel}$. In a case of three-dimensional systems, $\boldsymbol{k}_z$ dispersion is obtained from Eq. (2.22) which requires several measurements with excitation lights with different excitation energies. Angle-integrated photoelectron spectroscopy gives a density of states of electrons as the integral of the photoelectron spectra in a reciprocal space. There are two types of intensity distribution: one with respect to binding energies at a certain wavenumber is called energy distribution cuprate (EDC), and the other with respect to wavenumbers at a specific energy level is momentum distribution cuprate(MDC).

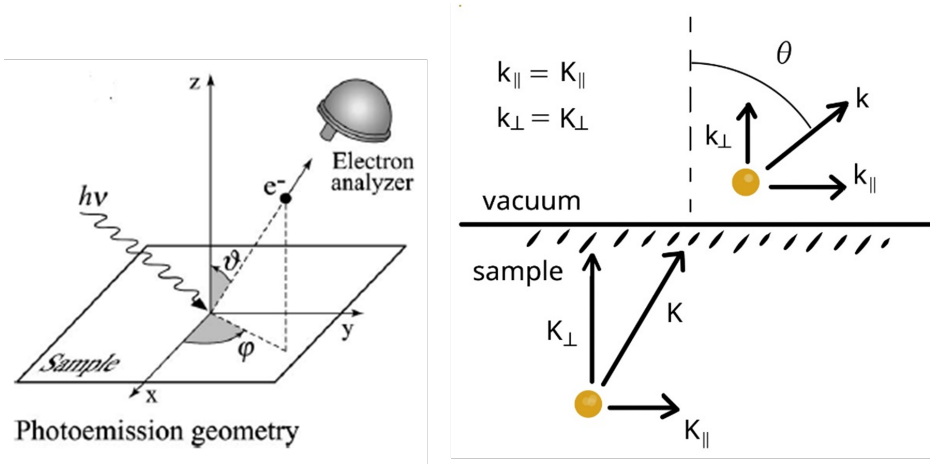

Figure 2.3: Geometry of ARPES measurements [24] (right) and momentum before and after an photoemission. Information of momentum is given through the polar angle θ. Momentum components parallel to the sample surface are conserved before and after photoemissions.

2.3 Mean escape depth of photoelectrons

In the photoemission process, excited electrons are affected from scatterings by other electrons and lattice during the transfer to the surface. The mean length between the surface and photoelectrons of the signal is called the mean escape depth and equal to the inelastic free mean path (IFMP), which is a distance scattered electrons move until the next inelastic scattering. This is settled by electron-electron scatterings dominant in a wide energy range, and its excitation energy dependence is know as the universal curve which is able to applied for a variety of materials extensively shown in Fig. 2.4 adopted from Ref. [26]. The higher energy range it enters to, the longer IMFP gets because the scattering cross section decreases. In the energy range lower than a phonon frequency, IMFP also gets longer even under the effects of electron-phonon scattering due to the absence of excitations of electron-electron scatterings. In our machine setup, there are two light sources of photon energies are 7 eV and 5.8 eV, which are in the ultraviolet region. Thus, the mean escape depth of photoelectron is expected to be of the order of 10-100 Åfor this excitation energy scale, and enables comparatively bulk sensitive measurements.

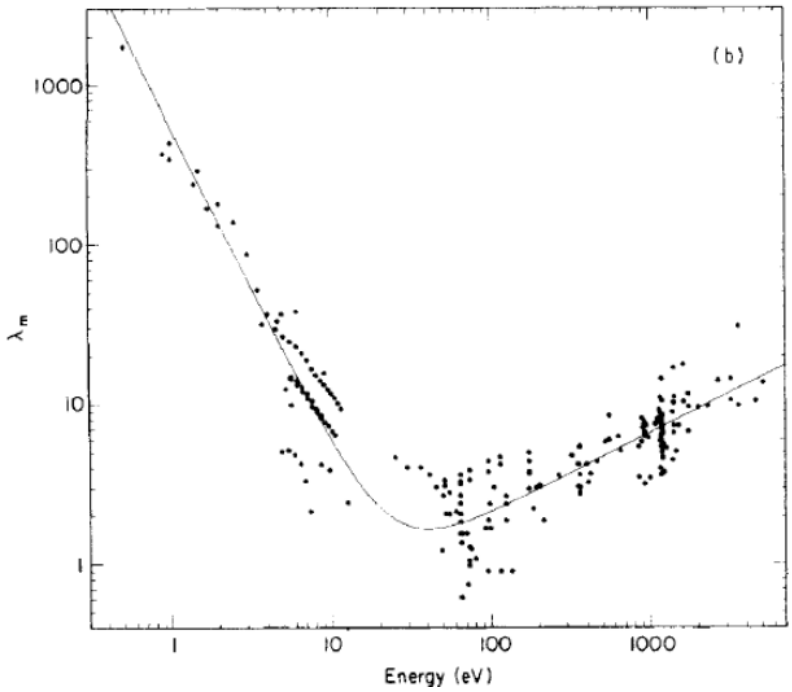

Figure 2.4: Mean escape depth of photoelectrons as a function of excitation energy. Measurements with an ultraviolet light of several eV are bulk sensitive where the depth is expected to be in the order of 10-100 Å[26].

2.4 Selection rule

In ARPES measurements, observed spectra are proportional to matrix elements as $I \propto |\langle f|A \cdot \widehat{p}|i\rangle|^2$ where $|i\rangle$ and $|f\rangle$ are the initial and final states respectively, A is the vector potential of polarized light and $\hat{p}$ is momentum operator of electrons, which is known as the orbital selection rule. Figure 2.5 shows a geometry of the ARPES machine system with a vertical slit as same as the configuration of our system. Taking account of the mirror plain along the direction of the slit, which is the yz plain in the figure, Spectra are observed when $|\langle f|A \cdot \widehat{p}|i\rangle|$ is an even function, and the final states are basically considered as a plain wave that is even to the mirror plain. This concludes that both of $A \cdot \widehat{p}$ and $|i\rangle$ should be even or odd to observe spectra.

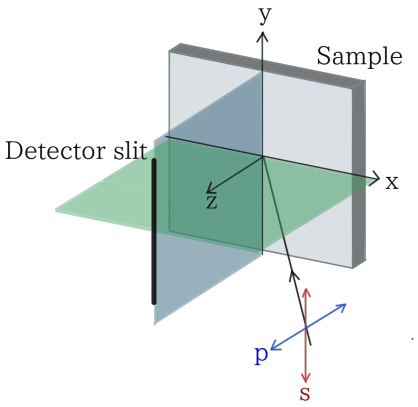

Figure 2.5: Geometry of the ARPES machine with a slit and a rotation axis in vertical. Observation of spectra contributed from different orbitals can be selected by switching direction of liner polarization of incident light.

2.5 Detection of photoelectrons

Photoelectrons emitted to a vacuum are taken in an electron detector. The right figure in Fig. 2.6 is a schematic of a hemispherical electron energy analyzer used in this study. After the emission, at first, photoelectrons pass through a electron lens which focuses on the position of a slit and accelerates/retards electrons to settle their energies in a path energy E_p. Then, inside of the hemisphere-shaped electrostatic sensor, induced voltage bends the path of photoelectrons and transports them to a micro-channel-plate (MCP) on which an image is formed with photoelectrons with energies $E_p \pm \delta E$. Photoelectrons amplified by the MCP incidents into a fluorescent plate and create bright spots whose counts and positions are observed by a CCD or sCMOS camera to obtain spectra. The capture angle of the slit is $\pm 15°$ so a dispersion along one direction in the wavenumber space can be observed without a sample rotation. The left of Fig. 2.6 shows the relation of energy levels between the sample and analyzer, and the path energy is given as the following,

$$E_p = E_{kin} + \Phi - \Phi_{ana} - eV_R, \tag{2.23}$$

where V_R is the retardation voltage and Φ_{ana} is the work function of the analyzer. There are two types of measurements: one is called a fix mode and the other is a swept mode. In the former method, V_R is fixed and photoelectrons with path energy E_p specific to each channel are detected, therefore it requires calibrations for every channels. In contrast, the latter method sweeps V_R and be able to measure in a wide energy range, which does not affected from an inhomogeneity of channels' sensitivity because it uses all channels for the detection for each energy whereas it elongates each scanning time.

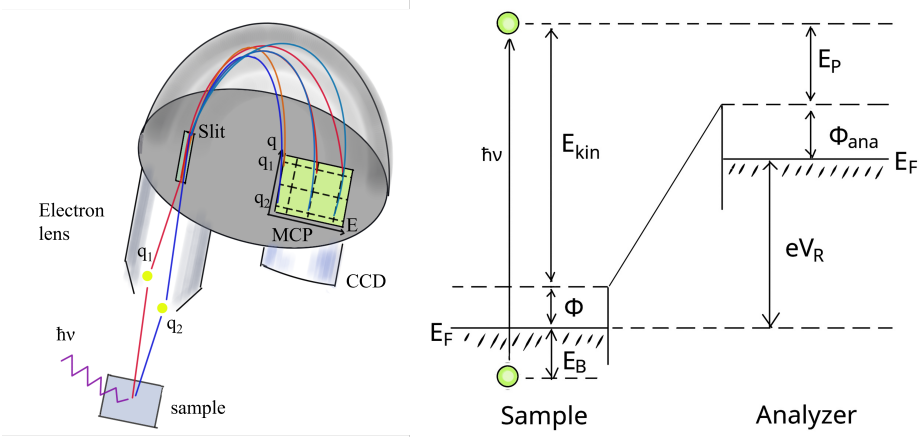

Figure 2.6: A schematic of a hemispherical electron energy analyzer (left) and relation of energy levels between samples and an analyzer (right). Photoelectrons are accelerated or retarded to settle their energies E_p by a electron lens, and amplified through a MCP. Then, the image formed on MCP is detected by a camera as bright spots on a fluorescent plate.

Chapter 3

Ultra-low temperature and ultra-high resolution laser ARPES

This chapter introduces the machine setup and describes experimental details including preparation of samples, bases of the methodology to attain the high resolution, and the background of the installation of the new light source.

3.1 Overview of the ARPES machine

The laser-ARPES apparatus used in this study is the ultra-low temperature and ultra-high resolution laser ARPES machine named the 3rd unit, which is shown the Fig. 3.1, whose lowest temperature and highest energy resolution are 1K and 70 μ eV respectively, holding the world record [27]. It contains the VG-Scienta HR8000 electron analyzer and the 6.994 eV quasi-continuous-wave laser. This light source is at first generated from the Coherent Paladin Compact 355-4000 which emits the third harmonic generation of an 1064nm fundamental wave of Nd : YVO_4 and its repetition ratio is 120 MHz. Through three sets of optics called loop path, we can maximize the repetition rate to 960 MHz. After that, the light enters to the wavelength-conversion component consisted from a nonlinear optical crystal $KBe_2BO_3F_2$ and two prisms of CaF_2 for the second harmonic generation, and then we finally obtain the 6.994 eV (177 nm in wavelength) excitation light.

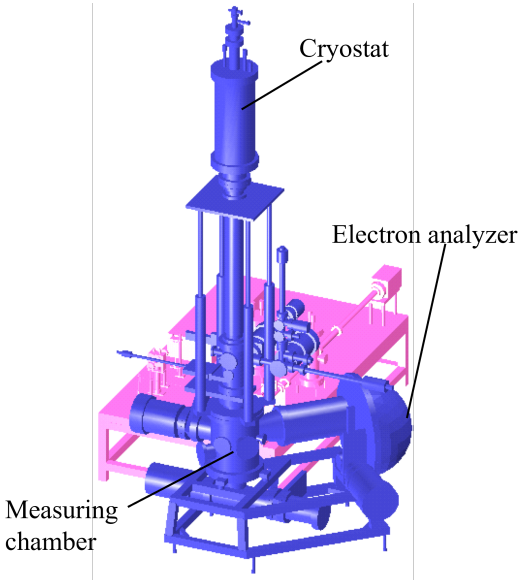

Figure 3.1: A schematic of the 3rd unit of ARPES machine. It consists of a cryostat, a hemispherical electron analyzer and 4 vacuum chambers: the main chamber for measurement, preparation chamber for cleavage, transfer chamber and bank chamber for inserting samples.

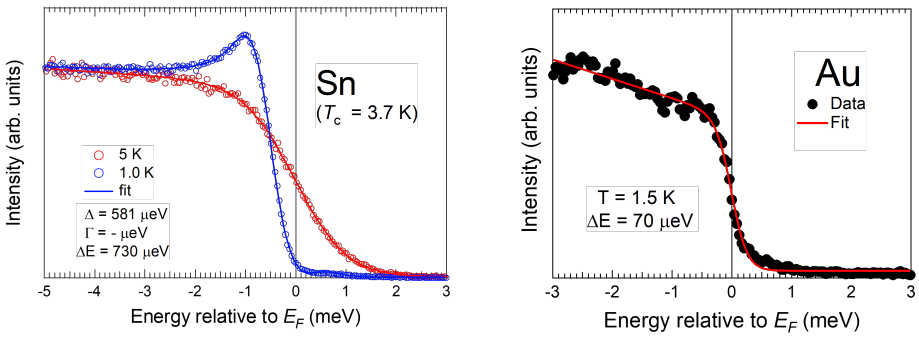

Figure 3.2: The lowest temperature is confirmed by the BCS fitting to the spectra of superconducting Sn (left) and the highest energy resolution is confirmed by the Fermi-edge fitting to the spectrum of Au which is convoluted considering a thermal broadening effect by a finite temperature $T = 1.5$K (right).

3.1.1 Sample preparation

For measurements in this machine, it is necessary to prepare samples in proper methods to put them in the main chamber correctly. We use sample holders of oxygen-free copper plates designed for the 3rd unit of ARPES machine, on which samples are mounted. Through the back of this plate, a sample attains thermal and electrical conductivity, so bad quality of its surface effects critically on the performance. To avoid this problem, the back side of the holder are polished with a several sandpapers of different granularity, basically from # 320 to # 2000. For mounting samples, a silver epoxy paste is used as a conductive glue. We used a two-component type which requires to mix two kinds of pastes in correct ratio and to heat up properly for hardening. Note that inappropriate heating process can oxidize the sample holder deteriorating its conductivity, which is easily identified from the colour at a glance. The oxidization makes Ef mismatch and the energy resolution decrease which can spoil whole measurements. Moreover, notice that the thermal conductivity of the top plate of heaters is not homogeneous and areas where heating belts lay get hotter locally than a set temperature. Considering above, there is usually several seats of Al foil and a glass seat of a few mm width which is also wrapped by Al foils at least twice between samples and the heater.

After putting samples on holders, a preparation for cleaving follows and there are classified roughly into two methods; cleaving with scotch tape or cleaving pins. The former can be applied for easy-cleaving samples such as layered materials or others bonded by weak force like van der Waals force. This method is completed instantly compared with the other way, but able to pollute inside of a chamber after the cleavage. From this perspective, it is conducted mainly in the transfer chamber which is far from the main chamber. The other methods, cleaving poles are mounted on samples which enable to cleave hard samples and to break materials without cleavability. Depending situations, there are alternatives for size and materials of poles and glues. In any case, pay great attention to their conductivity because insulating pins and glues are left on the bottom of the thermal shield surrounding the sample position after cleaving, and then it makes inhomogeneous fields to distort the trajectory of photoelectrons. This problem requires to get rid of those insulators with opening the chamber, which takes at least a few weeks to recover, so insulators on a sample holder should be entirely covered with a conductive carbon black spray in order to ensure its conductivity.

For small samples, it is recommended to use a thin wire whose diameter is 100 μm to put silver paste on samples. When the wire is dipped into a pot of silver paste, a thin spike of paste is sometimes formed at the point of the wire, so repeat to dip to get a spike thinner than the surface area of samples. Then, using a optical microscope, put it on samples and stand cleaving pins, whose diameter is selected 1 mm typically to make it easy to stand. Though the pin is larger than the area covered with silver paste, there is no problem because they touch only through the glue.

3.2 Energy resolution

Theoretical energy resolution is written in

$$\Delta E_{tot} = \sqrt{(\Delta E_{ana})^2 + (\Delta E_{h\nu})^2 + (\Delta E_{etc})^2}, \tag{3.1}$$

where ΔE_{tot} is a theoretical value of resolution of an analyzer, and ΔE_{ana} is FWHM of the energy of the light source [28]. ΔE_{etc} in the last term in the square root represents generalized effects from external conditions i.e., electric stability of a power source such as condition of the ground, working accuracy in the manufacturing process of analyzers, etc.

It is required sufficiently high energy resolution to observe tiny gap structures of unconventional superconductors, which have not been revealed because their extremely low T_c prevents us from approaches by ARPES. Superconductors showing non-BCS-like behavior includes plenty of superconductors whose T_c is the order of 1 in an absolute temperature, as shown in Fig. 3.3. It is notable that they contains a variety of fascinating states such as inversion or time reversal symmetry breaking ones, heavy fermion system and candidates of topological superconductors. Thus, direct observations of superconducting gaps in this machine system plays a significant role to pave the way to understanding of the mechanism of superconductivity. in addition, of course, this also can be a strong method to study low-energy scale phenomena other than superconducting phases.

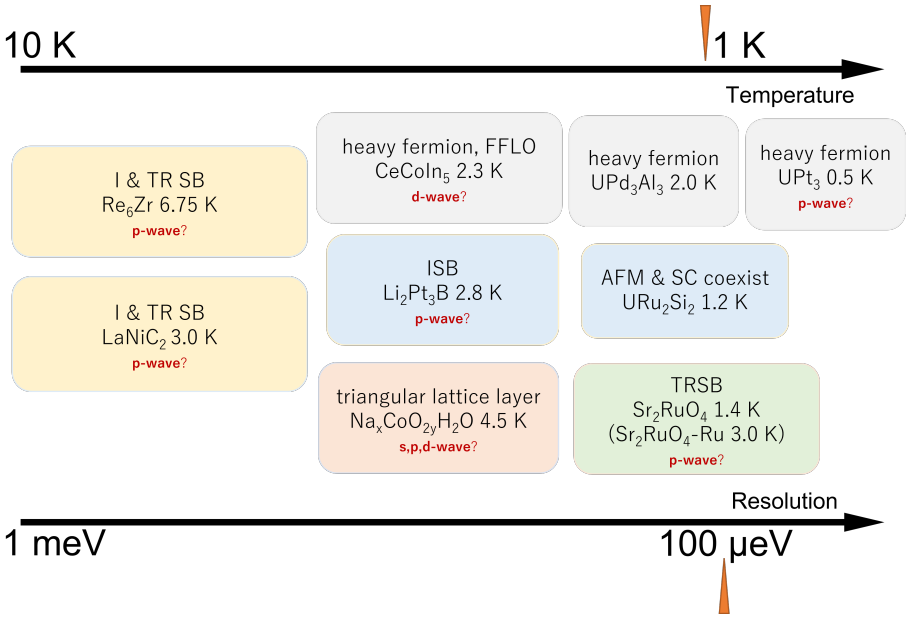

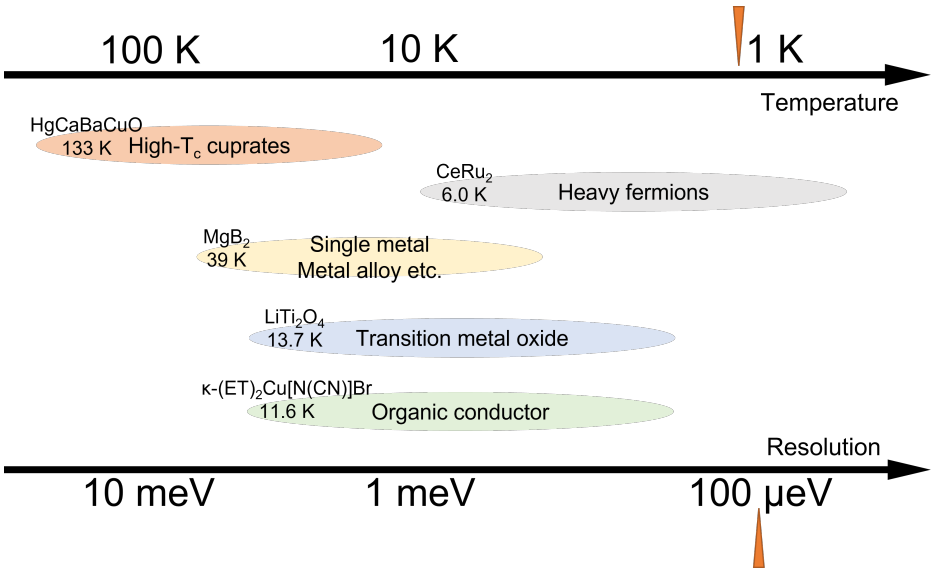

Figure 3.3: Candidates of samples.

3.3 Realization of high energy resolution

3.3.1 Cooling

本項の内容は特許申請のため、インターネットでの公表をすることができません。

3.3.2 Theoretical value of energy resolution of an electron analyzer

A theoretical value of energy resolution of a hemispherical electron analyzer is given as

$$\Delta E_{ana} = \frac{\omega E_p}{2R}, \tag{3.2}$$

where ω and R are the width of slits and radius of a hemispherical analyzer and E_p is a path energy [23]. To improve this value, it is effective to shrink the slit size and path energy and to expand the radius of the analyzer but they also affect on photoelectron counts, and then there is a trade-off between resolution and efficiency of a measurement. In our system, the lowest set value of the path energy is 0.5 eV and one of slit size is 50 μm. However, the narrower a slit is designed for high resolution the more difficult it becomes to manufacture, which can cause deterioration of the processing accuracy and eventually leads lower resolution. The radius of the analyzer we used is 200 mm.

3.3.3 Theoretical value of energy resolution from light sources

AtTheoretical value of energy resolution from light source is determined by the FWHM of the photon energy. The line width of the 7 V laser in our lab is originally 260 μeV and can be improved to 25 μeV by installation of an etalon. This optical device consists of plates of fused silica set parallel and whose inner reflection planes have partially reflective coating. It can works as a wavelength selective filter outputting only lights with a certain wavelength which is reflected even number of times. The length of the light path in the device depends on temperature and the transmittance for each wavelength also deviates. To compensate it, the etalon is put in a chamber of N_2 atmosphere and its temperature is controlled with a heater. The reflection rate of the etalon is 80 % which attenuates the laser power of 3.5 eV to 1/10 of the original power measured just after the emission. This means the power of the second harmonic generation decrease to its power of two that is 1/100, which sacrifices the efficiency of measurements critically.

3.4 Problem and solution

3.4.1 Trade-off between high resolution and efficiency

The most serious problem of the machine was the incapability of practical use of the highest resolution setting that kills the measuring efficiency due to too low photoelectron counts. This setting takes long time for at least 7 hours to measure one spectrum,

and actually has been used only for the test measurement of Au to evaluate the spec. The typical setting was as follows: a path energy was 1 eV and slit size is 0.5 mm, which is twice and ten times of the lowest value in each. In addition, because the etalon was taken out, the line width was 260 μeV whereas the power is 100 hundred times of the lowest value, which concludes the total resolution was 1.25 meV. From above, to enable the highest resolution measurement, it was requested to improve the efficiency by 2000 times estimated by a simple calculation.

3.4.2 Space charge effect

In spite of the requirement to manage inefficiency, there is another general problem lowering resolution due to a space charge effect caused by a high peak power of a pulse laser. Excessive photons arises photoemission instantly and the Coulomb resolution occurs among highly dense photoelectrons, which is the process of a space charge effect. This effect distorts the original trajectories of photoelectrons which contains the information of electronic states in solids, and finally lowers resolution [29] as shown in Fig. 3.4. To avoid this phenomenon, it is necessary to increase the repetition rate of the laser and decrease the peak power.

3.4.3 Solution

For the sake of the solution to these two points, there was demand to decrease the peak power of a laser to avoid a space charge effect, and at the same time to increase the mean power to improve efficiency of measurements. To clear this, because solutions with a pulse laser are faced limitations, it is suggested to use a continuous-wave (CW) laser. With CW oscillation, we can attain a negligibly narrow linewidth compared with finite one of a pulse laser and lower a peak power significantly. Nevertheless, it had not been realized to develope such a high intensity deep ultraviolet CW laser due to the difficulty of low efficiency of a wavelength conversion. Then, in this study, enhancement cavities were applied to convert the wavelength.

An enhancement cavity is one of types of external cavities effective for wavelength conversion of a laser with low peak intensity as a CW laser [30]. This optics is independent from parts of the seed light, which enable to adjustment easily, and also it has another advantage for a incident light is enhanced by a resonance when its wavelength was converted through a nonlinear optical crystals. Figure 3.5 shows some typical structures of an enhancement cavity. This study adopted especially the small type of bow-tie shape and stabilized it to advance conversion efficiency, which eventually developed a new high intensity deep ultraviolet CW laser.

To control the enhancement cavities, we used the Pound-Drever-Hall (PDH) method with a voice coil motor (VCM) [31–33]. Generally a light is absorbed in a cavity if it satisfy resonance condition, so detecting the reflection from a cavity and imposing modulation on the frequency to compensate its intensity, the light output is enhanced. However, intensity change of the reflected light includes contributions originated from

two types of fluctuations that is of intensity and frequency of the incident light, which prohibit the modulation on frequency by the intensity change [34]. In the PDH method, error signals are produced from the derivative of the intensity of the reflected light as a function of frequency, using which it modulates on frequency to stabilize resonant states.

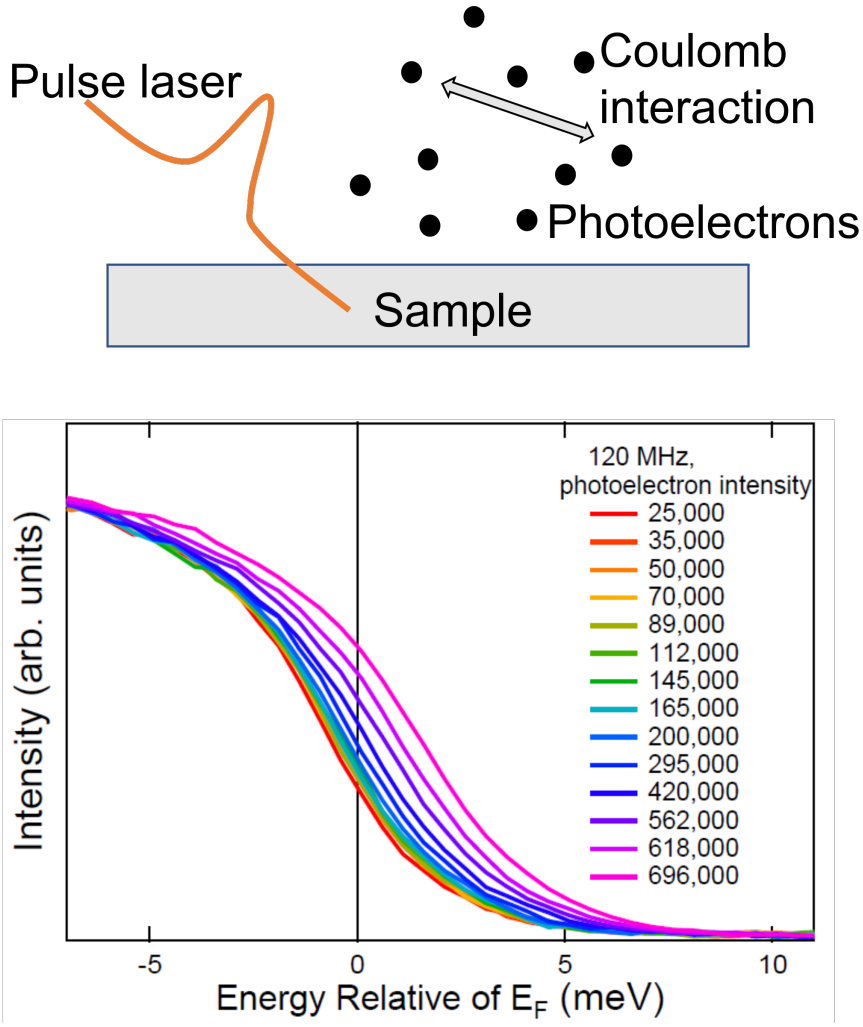

Figure 3.4: A process of space charge effect, that is high peak power of a pulse laser excite highly dense photoelectrons among which the Coulomb interaction affects the trajectories of photoelectron (up) and the power dependence of spectra (down). As the power increase the EDCs shift to the higher energy side and also broadened, which disable microscopic investigations

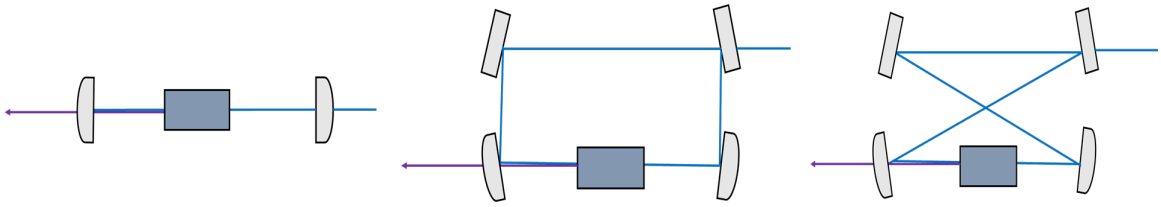

Figure 3.5: Schematics of a variety of optics of enhancement cavities. They describe line-, ring- and bow-tie-shaped ones from left to right. In this study, bow-tie shaped cavity was adopted on account of its compactness

Chapter 4

Installation of the new light source

The new high intensity CW laser was developed and installed with an aim to realize the practical highest resolution measurement improving the low efficiency. Establishing the machine system with the new light source and stabilizing it, measurements for some low T_c superconductors were successfully performed.

4.1 Back ground of the installation

To solve problems of the conventional light source, what we need is three characters; high mean intensity, narrow linewidth and low peak intensity.

The high intensity was attained by the stabilization of the control for the enhancement cavities as mentioned later. Also, a choice of a CW laser satisfied the conditions of a narrow linewidth and low peak intensity. It is noted that a linewidth is negligible compared with a finite one of a pulse laser, for an optical electric field of a CW laser is written in a sin function so its Fourier transformation, which gives a linewidth, behaves as a delta function theoretically. In addition, a peak intensity was suppressed significantly due to a CW laser and differs from one of the conventional pulse laser by 2 or 3 orders as described in Fig. 4.1.

Also, the wavelength of 177 nm (7 eV) was not adopted, because it requires KBBF crystals used for wavelength conversion in the conventional light source, whereas there is no spare due to the difficulty of its synthesis and device integration. Instead, using $\beta - BaB_2O_4$ (β-BBO) crystals made by Oxide corp. who is a co-developer, deep ultraviolet light of 213nm (5.8 eV) was attained. This wavelength is selected because it is near to the edge of the area where the conversion efficiency does not decrease for this crystal. Moreover, lowering photon energy secondarily improved momentum resolution and bulk sensitivity.

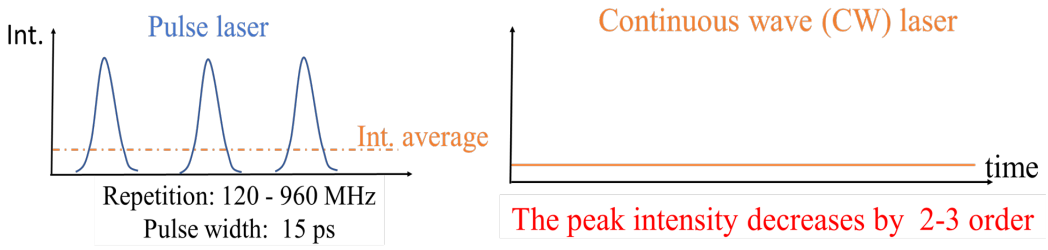

Figure 4.1: The difference in peak intensity of a pulse laser (left) and a CW laser (right). A pulse laser has instantly strong intensity and its order is more by 2-3 than a CW laser with the same mean intensity. This enable high energy resolution measurements in short scanning time with a CW laser which has so weak peak intensity that a space charge effect is dramatically suppressed.

4.2 Development and installation

本項の内容は特許申請のため、インターネットでの公表をすることができません。

4.3 Angle-integrated photoemission spectroscopy

本項の内容は特許申請のため、インターネットでの公表をすることができません。

4.4 Angle-resolved photoemission spectroscopy

本項の内容は特許申請のため、インターネットでの公表をすることができません。

4.5 Observation of the gap of $LaNiC_2$

本項の内容は特許申請のため、インターネットでの公表をすることができません。

4.6 Further improvement and conditions for practical use

本項の内容は特許申請のため、インターネットでの公表をすることができません。

4.7 Summary

本項の内容は特許申請のため、インターネットでの公表をすることができません。

Chapter 5

Novel superconducting states in the tetragonal phase of Fe(Se,S)

5.1 Previous research

5.1.1 Introduction of the parent material FeSe

The superconductivity of FeSe was found with $T_c \sim 8$ K in 2008 [35], and has fascinated a plenty of studies for increase of T_c to 36.7 K under high pressure 8.9 GP [36]. In addition, further increase of T_c more than 50 K was reported in a monolayer FeSe thin film grown on $SrTiO_3(001)$ [37]. From these results, this material was classified to another new material group expected as high T_c superconductors than cuprates.

Among iron based superconductors, FeSe has the simplest crystal structure consisted of layers of Fe and Se where these atoms exist one by one from top-view as shown in Fig. 5.1.

The original crystal structure of FeSe holds 4-fold rotational (C_4) symmetry, but it exhibits a structural transition from tetragonal to orthorhombic structure at $T_s \sim 90$ K [38]. This type of transition, which preserves translational symmetry but breaks break rotational symmetry, is called a nematic transition named from analogy to liquid crystal. Such a state is also known to realize in other iron-based superconductors like iron-pnictides as an electronic nematic transition originated from splitting of d_{zx} and d_{yz} orbitals [39], whereas they exhibits also a spin-density-wave (SDW) phase which vanishes on an antiferromagnetic (AFM) quantum critical point (QCP)[40]. Generally a superconducting dome in the phase diagram has a peak around QCP, but the overlapping of SDW and nematic phases makes the relationship between superconductivity and QCP too complicated to research. On the other hand, FeSe shows no AFM order which is confirmed by temperature-dependent Mössbauer spectra across T_s [38], and therefore this system has been regarded an ideal platform to study the relation between nematicity and superconductivity.

The band dispersion were observed directly in a several ARPES studies utilizing

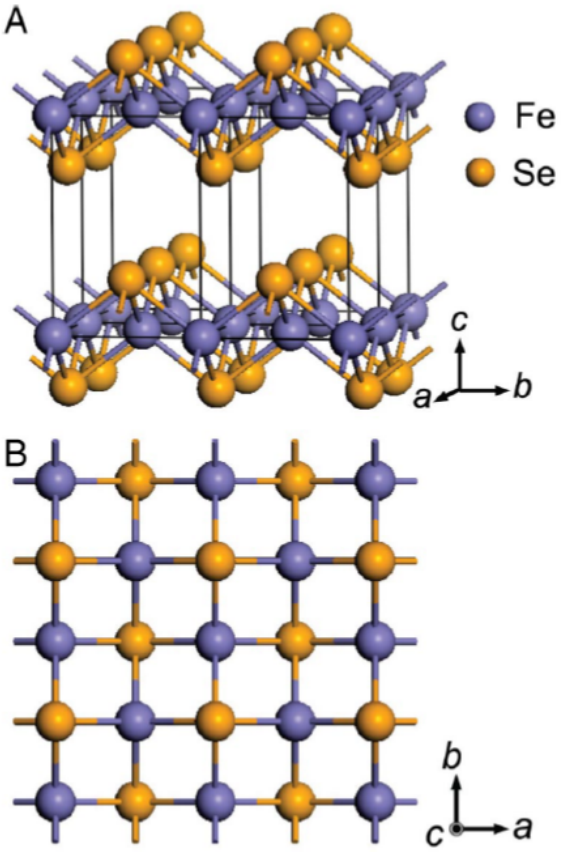

Figure 5.1: Schematic crystal structure of FeSe from (a) side-view (b) top-view. Fe and Se atoms exist one by one creating layers [35].

a detwinning technique with strain [41–45] and it is known to exist hole pockets around the center and electron pockets around the zone corners as shown in Figs. 5.2. In contrast to the DFT calculations predicting three hole pockets around the Brillouin-zone center, the observed FS shows only two hole pockets in the tetragonal phase. In addition, the actual FS is smaller and flatter due to renormalization with orbital-dependent factors than the calculated one. Below T_{s}, one of the hole pockets disappears because it is lifted above the Fermi level by the splitting between the d_{zx} and d_{yz} orbitals induced by orbital ordering.

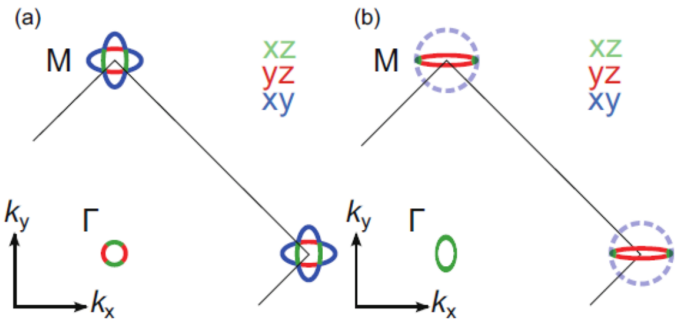

Figure 5.2: Schematic Fermi surface of detwinned FeSe obtained from ARPES [43]. (a) the case of the tetragonal phase (b) the case of the orthorhombic phase.

5.1.2 Superconducting state

The effect on the SC state from nematic domains was studied in STM and ARPES measurements [41, 46, 47].

The STM results shown in Figs. 5.3 indicate the existence of an additional gap around the twin boundaries showing V-shaped spectra. On the other hand, no zero-bias peak was confirmed around the boundaries although the sign change in one of the gap components should give total gap closing if the induced gap component is real. Therefore, these behaviors are interpreted as time reversal broken superconductivity whose gap contains imaginary parts.

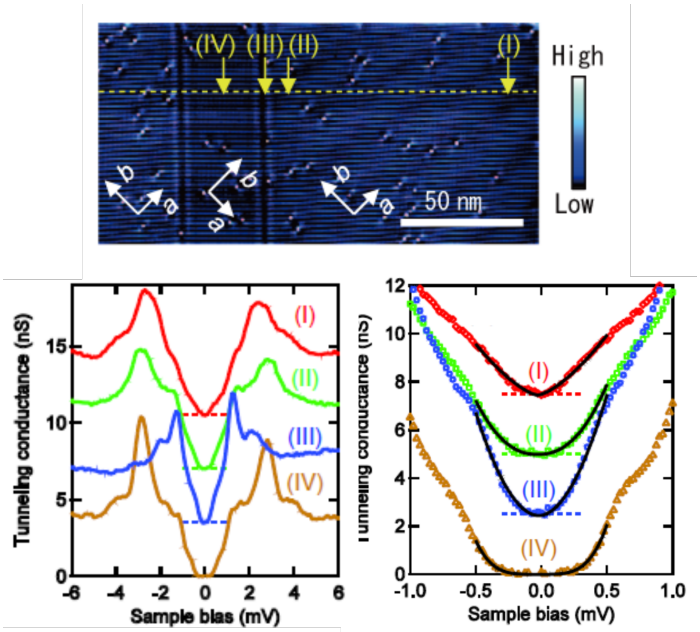

Figure 5.3: Time reversal symmetry broken superconductivity induced by twin boundaries. (top) STM image at 1.5 K with double twin boundary. (bottom left) tunneling spectra (bottom right) high resolution tunneling spectra and fitting curves [46].

In ARPES studies, 2-fold symmetric gap anisotropy was reported and the direction of nodes in the FS depends on that of a nematic domain. As shown in Figs. 5.4, elliptical FSs are confirmed and the direction of a major axis reflects the condition of nematic domain structure confirmed by polarization microscopy. Anisotropic superconducting gap with C_2 symmetry was observed with gap nodes in the direction of long axis and it is suggested that two nodes exist in a narrow FS angle range and there are actually four nodes in the FS of a single domain for exclusion of $p-$wave superconductivity.

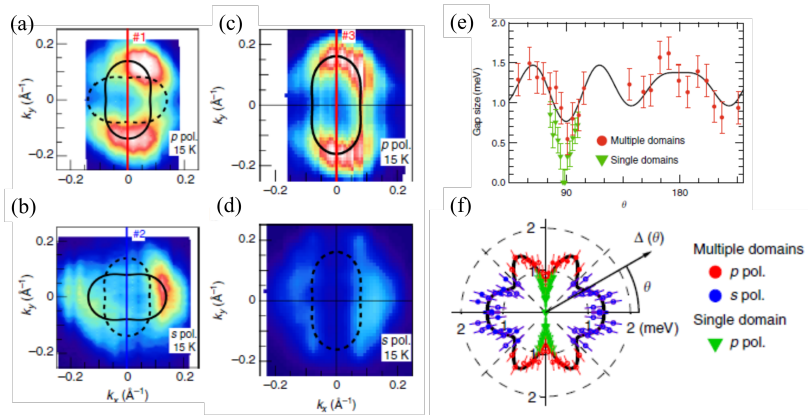

Figure 5.4: Results of ARPES measurements for single crystals of FeSe. (a), (b) FS mapping measured with p-polarized light and s-polarized light respectively on a twin domain surface. (c), (d) Same as (a) and (b) but measured on a single domain surface. (e) Plots of estimated gap sizes as a function of FS angle θ and fitting curve (f) superconducting gap anisotropy in a circle graph [41].

5.1.3 Phase diagram and nematic critical point of Fe(Se,S)

Nematicity can be tuned by the isovalent substitution of Se for S changing the $a-$axis and $c-$axis lattice constants and the height of chalcogen atoms from Fe planes whereas high pressure does not change the height. Induced by high pressure, the nematic phase is suppressed but it is followed by entrance to a SDW phase whereas it disappears at $x = 0.17$ without any magnetic orders as shown in Fig. 5.5 [48].

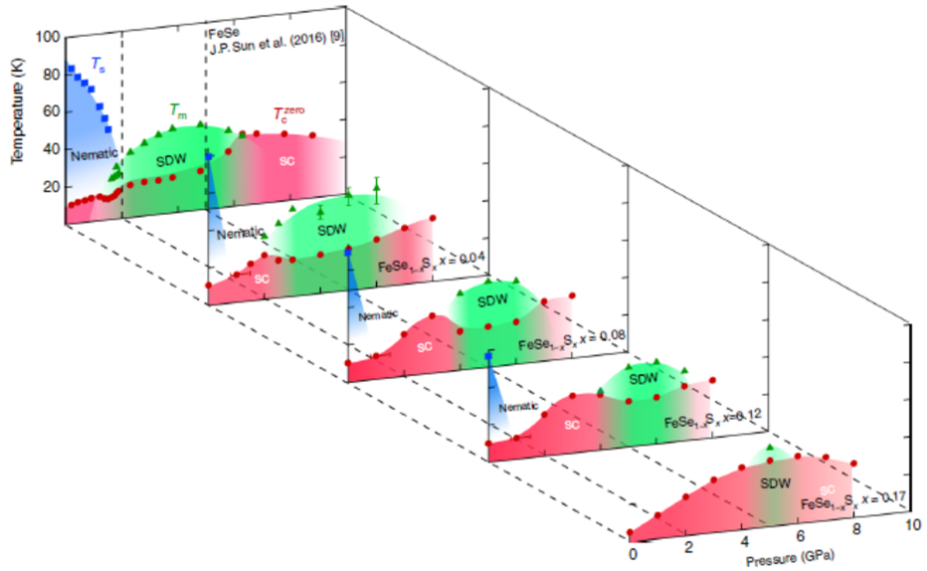

Figure 5.5: T-p-x phase diagram of $FeSe_{1-x}S_x$. nematicity is suppressed by S-substitution and disappears at $x = 0.17$ showing no magnetic phase.[48]

Elastoresistance measurements found that the nematic fluctuation diverges at the nematic critical point (NCP) $x = 0.17$ [49], which is probed as temperature dependent nematic susceptibility obtained by the elastoresistance measurements using piezoelectric devices [50]. As shown Fig. 5.6, T_s and the Weiss temperature T_θ obtained from analogy to magnetic susceptibility reach to 0 K and nematic susceptibility diverges at $x = 0.17$ that corresponds to the NCP.

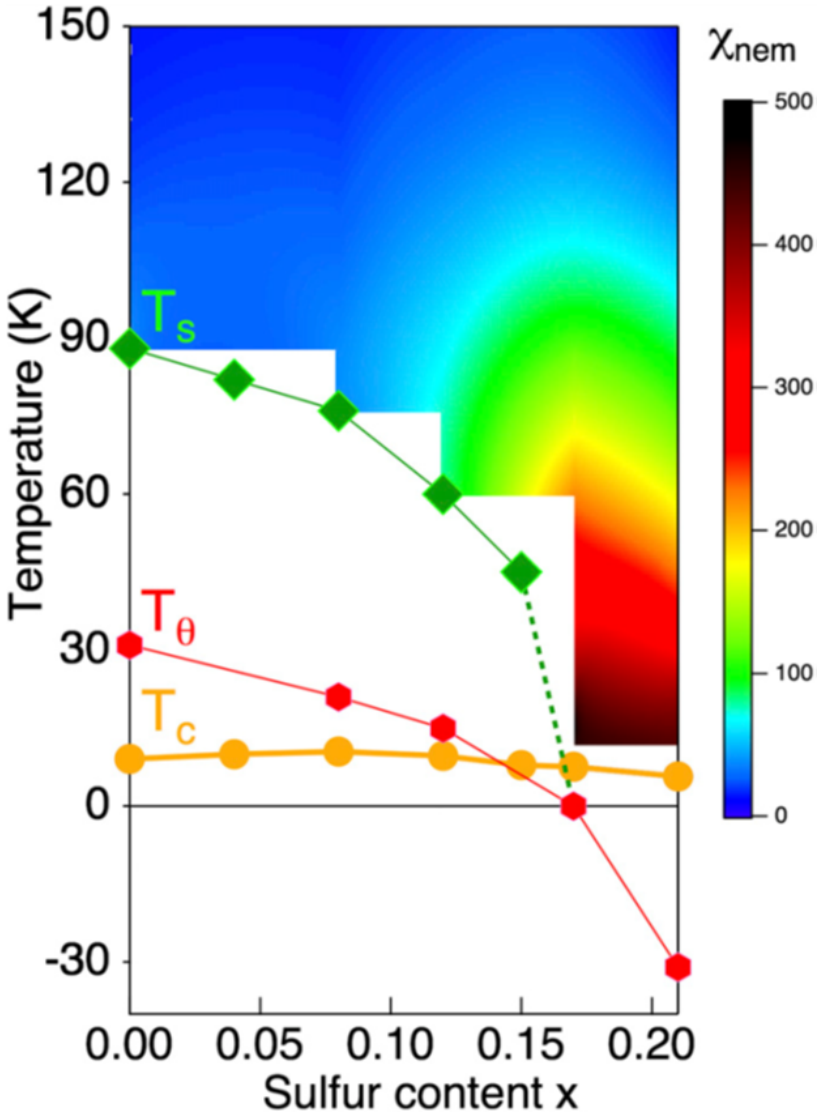

Figure 5.6: Phase diagram and nematic criticality of $FeSe_{1-x}S_x$ system [49]. T_s and the Weiss temperature T_θ obtained from analogy to magnetic susceptibility reach to 0 K and nematic susceptibility diverges at $x = 0.17$ that corresponds to the nematic QCP.

5.1.4 Specific heat and thermal conductivity

Specific measurements for $FeSe_{1-x}S_x$ observed a significant change in superconducting states depending on nematicity [51]. Figure 5.7 shows the temperature dependence of the electronic component of the specific heat and the field dependent specific heat. From the former, the finite Sommerfeld coefficient was confirmed only in the tetragonal phase and the latter shows the $\sqrt{H}$ behavior of specific heat indicating the existence of line nodes in tetragonal phase whereas it is linear with H, which is a character of full gap superconductivity, in the nematic phase. Moreover, T_c decreases to ~ 4.5 K in the tetragonal phase from ~ 10 K in the nematic phase. Thus, it is expected to realize a distinctly different SC state with a negligible residual DOS strongly affected from the nematic fluctuation.

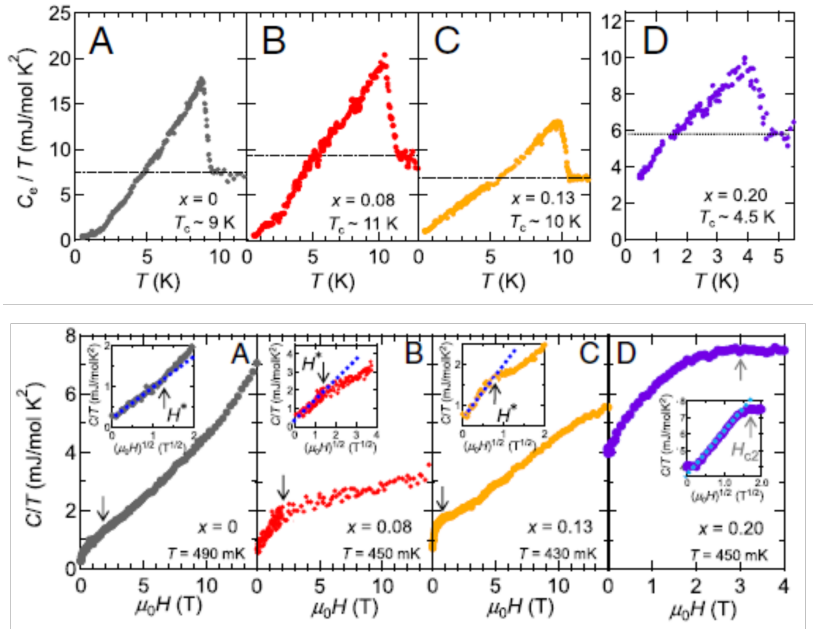

Figure 5.7: Abrupt change in superconducting states when crossing the nematic QCP [51]. Temperature dependence of the electronic component of specific heat (upper) and field dependent specific heat (below). A negligible finite Sommerfeld coefficient is recognized in the tetragonal phase. Moreover the behavior of specific heat with respect to field H also changes from linear dependent to proportional to $\sqrt{H}$.

5.1.5 STM measurements

In the STM measurements, it is confirmed that quasiparticle interference (QPI) patterns, which anisotropically and strongly reflect the nematicity, transform gradually to isotropic shapes as shown in Figs. 5.8 [52]. Moreover, tunneling spectra show apparent shrinkage of the superconducting gap amplitude when across the NCP, and at the same the zero energy spectral weight increases, which indicates finite DOS consistent to the specific measurements [51]

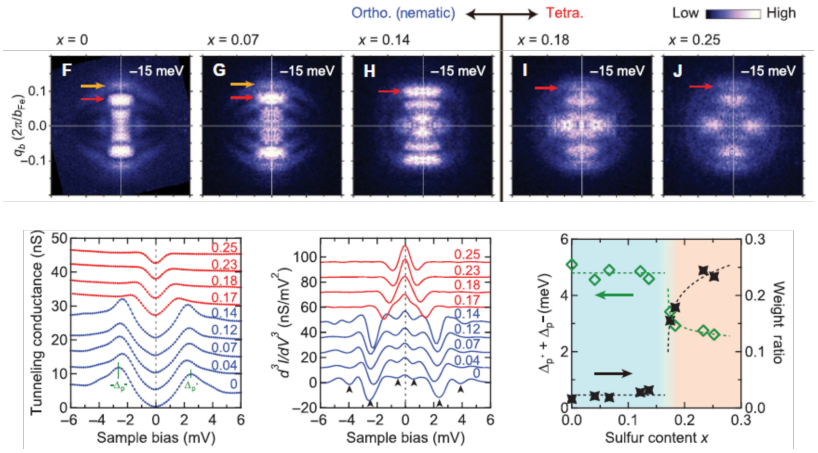

Figure 5.8: (upper)In-plane QPI patterns of $FeSe_{1-x}S_x$. (below) Tunneling spectra, their second derivatives, and substitution rate x dependence of gap amplitude and zero energy spectral weight [52]

.

5.1.6 BCS-BEC crossover

$FeSe_{1-x}S_x$ system is also expected as a platform for the crossover between weak coupling BCS regime and a strong coupling Bose-Einstein condensation (BEC) regime, where Cooper pairs are formed in a momentum space and real space, respectively. In the crossover regime, the ratio of coherence length referring to a size of a Cooper pair ξ to the average of inter-electron distance k_{F}^{-1} where k_{F} is Fermi momentum should be comparable, which imposes the relation between the pair condensation energy and Fermi energy as $\Delta/\epsilon_{\mathrm{F}} \approx 1$ [53]. In addition, strong superconducting fluctuation is expected to emerge with preformed pairs showing a pseudogap above T_{c}. Moreover, it is known that the Bogoliubov quasiparticle (BQP) band changes its shape depending on the strength of attraction, that is, it is downward convex, flat band, and upward convex in the BCS limit, crossover regime, and BEC regime, respectively.

This phenomenon was studied in ultracold atomic gas systems, where the interaction between two fermionic atoms can be controlled by utilizing a magnetic-field Feshbach resonance [54]. On the other hand, it is difficult to tune interactions between fermions in solids, which prevents from its realization generally.

A previous ARPES study for $FeSe_{1-x}S_x$ observed the BQP bands transformed from BCS-like behavior to that of BEC by S substitution. In the tetragonal phase, the band dispersion shows a BEC-like upward convex shape, and in addition it was confirmed that gaps open above T_{c} as shown in Figs. 5.9 [55]. On the other hand, estimated $\Delta/\epsilon_{\mathrm{F}}$ decreases as S content x increases against the theory mentioned above. This contradiction was explained as the consequence of the multiband character, that is, the interband coupling between the α band crossing E_{F} and the β band below E_{F} get close because the latter band rises when the nematicity suppressed.

Heat capacity, STM, and magnetic torque measurements also supported the BCS-BEC crossover in this system [56], which reported continuous C_e/T behaviors at T_{c} reminiscent of the BEC transition in the Bose gas systems, and strong superconducting fluctuation as affected by preforming pairs though the BEC in multiband systems is different from that of single band systems, which expects emergence of a pseudogap.

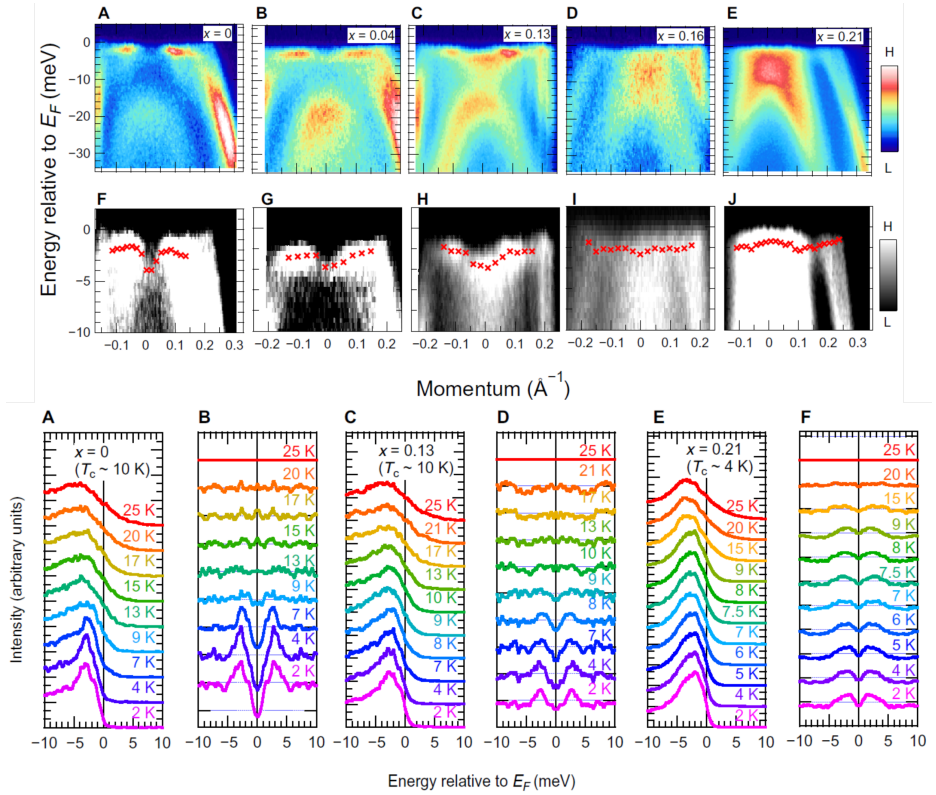

Figure 5.9: BCS-BEC crossover in $FeSe_{1-x}S_x$. (upper)BQP band dispersions of each composition. (middle) Peak positions of BQP band dispersions. With low S content x the dispersion behave as BCS regime, which is transformed to flat as x increases entering to the BCS-BEC crossover regime, and becomes upward convex in tetragonal phase as though the system moves to the BEC regime. (below) Temperature dependent EDCs for each x. In the tetragonal phase, gaps open above $T_c \sim 4$ K [55]

5.1.7 muSR measurements

Recent muSR studies reported the time reversal symmetry broken (TRSB) superconductivity in the $FeSe_{1-x}S_x$ system by observations of spontaneous magnetic field only below T_c, which is not due to twin boundary [57, 58].

5.1.8 Ultranodal pair states

Recently, realization of a novel type of nodal superconductivity is expected in time reversal symmetry breaking systems and studied well mainly from a theoretical point of view [18, 58–61]. Conventionally, the nodal superconducting states have been classified into two types, point nodes and line nodes. Literally these mean the shape of the nodal regions in k- space such that nodes exist at points for the former or along lines for the latter. In the novel nodal states, however, nodes form new surfaces called Bogoliubov fermi surface, which consists of Bogoliubov quasiparticle excitations, distinguished from original Fermi surfaces in normal states.

To lead this state, it is required to antisymmetrize the Bogoliubov-de Gennes Hamiltonian $H(\mathbf{k})$ as $\tilde{H}(\mathbf{k})$ and define the Pfaffian $P(k) = \mathrm{Pf}\tilde{H}(\mathbf{k})$ which enables the discussion of topology of gap nodes characterized by the $\mathbb{Z}_2$ invariant. In multiband and TRSB systems, the Pfaffian can be negative in certain area in k- space. If there is sign changes of $P(\mathbf{k})$, it is required to exist the region with $P(\mathbf{k}) = 0$ in a momentum space between the regions with positive and negative $P(\mathbf{k})$. In addition, considering a property of the Pfaffian such as $\det H(\mathbf{k}) = P^2(\mathbf{k})$, zeros of the Pfaffian means the existence of zero energy states of $H(\mathbf{k})$. Therefore, the sign change of $P(\mathbf{k})$ means emergence of BFS, and we can treat $(-1)^l = \mathrm{sgn}\left[P\left(\mathbf{k}_-\right)P\left(\mathbf{k}_+\right)\right]$, where $\mathbf{k}_{+(-)}$ is the momentum inside(outside) the Fermi surface, as the Z_2 invariant. In the case that the Pfaffian has the zeros of even multiplicity, there is no sign change of $P(\mathbf{k})$ and it gives point or line nodes. In multiband systems, interband paring works as pseudo magnetic field to inflate such nodes and create new surfaces, whose example is shown in ref 5.10 [18].

5.1.9 Ultranodal states in $FeSe_{1-x}S_x$

Recently, it has been suggested that the ultranodal states with BFS is realized in the $FeSe_{1-x}S_x$ system on the assumption of TRSB and additional degree of freedom of multiband systems, which allows novel SC states in terms of the Pauli principle such as odd parity-spin singlet and even parity-spin triplet pairing structures [62]. Figures 5.11 show the evolution of BFS as the isotropic gap component on each pockets decreases and behaviors of specific heat and tunneling conductance indicating increase of the zero-energy value of the DOS. These are reminiscent of experimental results reported in Ref. [51, 52].

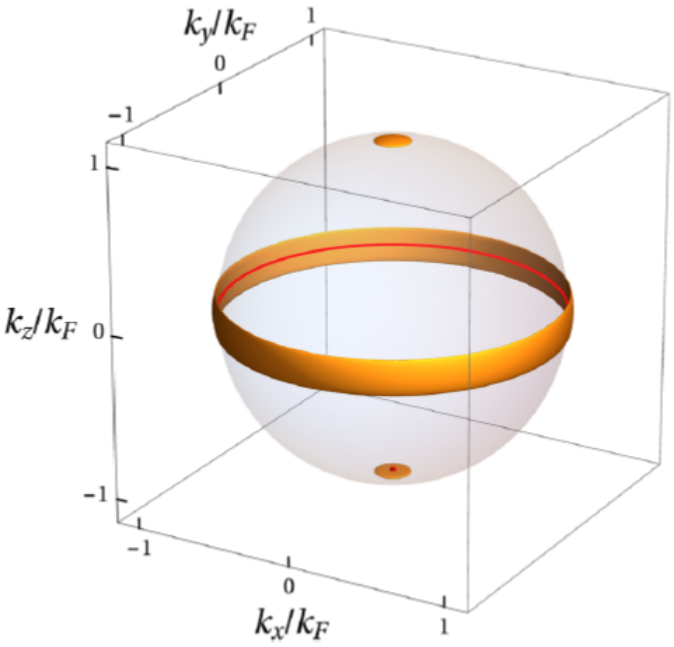

Figure 5.10: Schematic of BFS. The gray and semitransparent part represents a spherical FS in normal states. The red line and points are line and point nodes respectively in single band systems. In multiband systems, these nodes can be inflated by interband paring working as pseudo magnetic field, which leads emergence of BFS as represented with orange areas [18]

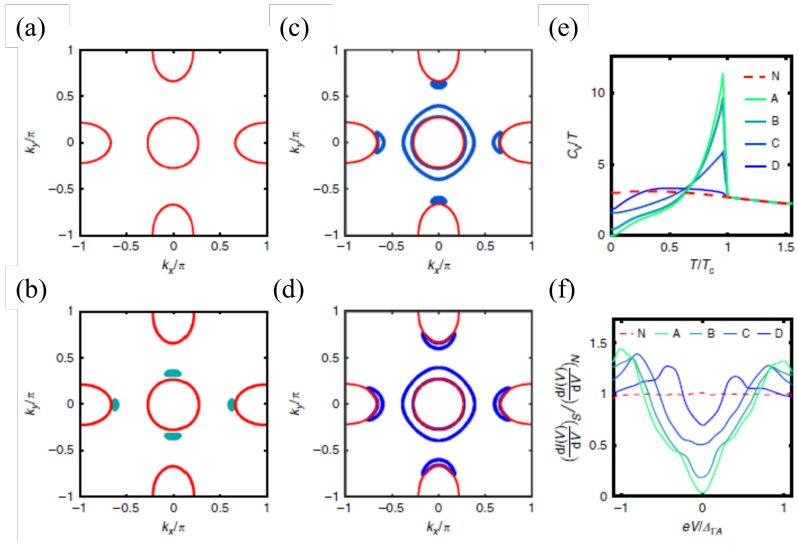

Figure 5.11: Ultranodal states expected to realize in the $FeSe_{1-x}S_x$ system [62]. (a)-(d) FSs of normal state (red contour) and BFS in SC states (blue/green patches) for different rate of the isotropic gap component to the anisotropic gap component on each pocket. (e) Temperature dependence of the specific heat for normal state in the dashed line and for SC states with the sets of isotropic gap parameters in each pocket. (f) The tunneling conductance for the same sets.

5.2 Motivation and Experiment

As described above, the tetragonal phase of the $FeSe_{1-x}S_x$ system is expected to exhibit superconducting states different from that in the nematic phase where the gap anisotropy is strongly influenced by nematicity. Also, there is no magnetic order induced by S substitution, so it is intriguing how the SC states are affected from the NCP. Moreover, it is suggested to realize ultranodal states with BFS which will be shown in the electronic states on $E_{\rm F}$. From these perspectives, we preformed laser ARPES measurements to observe the superconducting gap structure of 22 % S-substituted FeSe focusing on the hole FS around the center of the Brillouin zone.

Single crystals of $FeSe_{0.78}S_{0.22}$ were grown by the chemical vapor transport technique [63]. The details of the crystal growth are described in Ref. [49, 51]. ARPES data were collected by using a laser-ARPES apparatus developed at ISSP with the 6.994 eV quasi-continuous-wave laser (repetition rate: 960 MHz), and the Scienta Omicron HR8000 electron analyzer. The overall energy resolution was set to ${}^s im$ 1.3 meV with P.E. = 1 eV for most of measurements and the angular resolution was 0.1 deg. The Fermi edge of evaporated gold was measured to determine the $E_{\rm F}$ energy positions whose stability determines the error bars of the SC gap evaluated to be 0.2 meV originated by deviation of the ground. We confirmed that the obtained band dispersions were in agreement with the previous ARPES study of the Fe(Se,S) in the tetragonal phase [55].

Figure 5.12 shows the geometry of the manipulator on which samples are mounted and describes how it detects signals separating contribution from different orbitals. As explained in Chap. 2, the matrix element with even parity gives spectral intensity and it can be switched by polarization of incident light. Table 5.1 shows correspondence between the vector potential and observed orbitals in each direction. In our configuration, spectra from d_{yz} and d_{zx} are mainly obtained by s- and p-polarized light respectively [64].

Table 5.1: Orbital selection for the experiments in this study. Basically, in our configuration, s- and p-polarized light corresponds to the vector potential A_y and A_x respectively, but note that the latter can contain A_z depending on situations [64].

polarization	Orbitals with non zero $\langle f \vert \boldsymbol{A} \cdot \widehat{\boldsymbol{p}} \vert i \rangle$	
	$(\boldsymbol{k} \neq 0)$	$(\boldsymbol{k} = 0)$
A_x	d_{zx}	d_{zx}
A_y	d_{yz}	d_{yz}
A_z	d_{yz}	

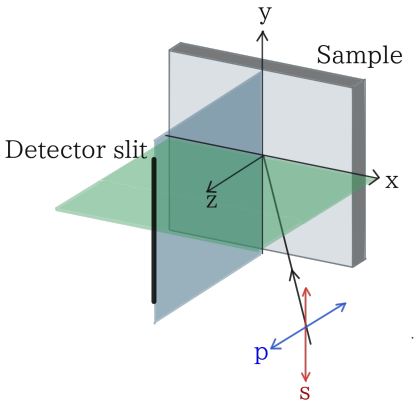

Figure 5.12: Geometry in our machine system. Because the direction of the slit is vertical the yz plain is adopted as a mirror plain on which the parity of matrix elements is determined to select orbitals contributing to observed spectral intensity, and this can be switched the direction of polarization of the incident light.

5.3 Results

本項の内容は、投稿論文の形で刊行される予定であるため、学位授与日から 5 年間インターネットでの公表をすることができません。

5.4 Discussion

本項の内容は、投稿論文の形で刊行される予定であるため、学位授与日から 5 年間インターネットでの公表をすることができません。

5.5 Summary

本項の内容は、投稿論文の形で刊行される予定であるため、学位授与日から 5 年間インターネットでの公表をすることができません。

Chapter 6

Conclusion

本項の内容は、投稿論文の形で刊行される予定であるため、学位授与日から 5 年間インターネットでの公表をすることができません。

Bibliography

[1]J. Bardeen, L. N. Cooper, and J. R. Schrieffer, "Theory of superconductivity", Phys. Rev. **108**, 1175–1204 (1957), https://link.aps.org/doi/10.1103/PhysRev.108.1175.

[2]斯波弘行, **固体の電子論**, パリティ物理学コース (丸善, 1996), https://books.google.co.jp/books?id=fSrJAAAACAAJ.

[3]C. C. Tsuei and J. R. Kirtley, "Pairing symmetry in cuprate superconductors", Rev. Mod. Phys. **72**, 969–1016 (2000), https://link.aps.org/doi/10.1103/RevModPhys.72.969.

[4]G. R. Stewart, Z. Fisk, J. O. Willis, and J. L. Smith, "Possibility of coexistence of bulk superconductivity and spin fluctuations in uPt_3", Phys. Rev. Lett. **52**, 679–682 (1984), https://link.aps.org/doi/10.1103/PhysRevLett.52.679.

[5]Y. Maeno, H. Hashimoto, K. Yoshida, S. Nishizaki, T. Fujita, J. G. Bednorz, and F. Lichtenberg, "Superconductivity in a layered perovskite without copper", Nature **372**, 532–534 (1994), https://www.nature.com/articles/372532a0.

[6]P. A. Frigeri, D. F. Agterberg, I. Milat, and M. Sigrist, "Phenomenological theory of the s-wave state in superconductors without an inversion center", The European Physical Journal B - Condensed Matter and Complex Systems **54**, 435–448 (2006), https://doi.org/10.1140/epjb/e2007-00019-5.

[7]林伸彦 and M. Sigrist, "解説：空間反転対称性のない系での超伝導", 固体物理 **41**, 1–14 (2006).

[8]P. A. Frigeri, D. F. Agterberg, I. Milat, and M. Sigrist, "Superconductors without an inversion center of symmetry: the s-wave state", arXiv:cond-mat/0505108, arXiv:cond-mat/0505108 (2005), http://arxiv.org/abs/cond-mat/0505108.

[9]A. D. Hillier, J. Quintanilla, and R. Cywinski, "Evidence for time-reversal symmetry breaking in the noncentrosymmetric superconductor $LaNiC_2$", Phys. Rev. Lett. **102**, 117007 (2009), https://link.aps.org/doi/10.1103/PhysRevLett.102.117007.

[10]T. Shang, M. Smidman, S. K. Ghosh, C. Baines, L. J. Chang, D. J. Gawryluk, J. A. T. Barker, R. P. Singh, D. M. Paul, G. Balakrishnan, E. Pomjakushina, M. Shi, M. Medarde, A. D. Hillier, H. Q. Yuan, J. Quintanilla, J. Mesot, and T. Shiroka, "Time-reversal symmetry breaking in re-based superconductors", Phys. Rev. Lett. **121**, 257002 (2018), https://link.aps.org/doi/10.1103/PhysRevLett.121.257002.

[11]A. D. Hillier, J. Quintanilla, B. Mazidian, J. F. Annett, and R. Cywinski, "Nonunitary triplet pairing in the centrosymmetric superconductor $LaNiGa_2$", Phys. Rev. Lett. **109**, 097001 (2012), https://link.aps.org/doi/10.1103/PhysRevLett.109.097001.

[12]G. M. Luke, A. Keren, L. P. Le, W. D. Wu, Y. J. Uemura, D. A. Bonn, L. Taillefer, and J. D. Garrett, "Muon spin relaxation in UPt_3", Phys. Rev. Lett. **71**, 1466–1469 (1993), https://link.aps.org/doi/10.1103/PhysRevLett.71.1466.

[13]G. M. Luke, Y. Fudamoto, K. M. Kojima, M. I. Larkin, J. Merrin, B. Nachumi, Y. J. Uemura, Y. Maeno, Z. Q. Mao, Y. Mori, H. Nakamura, and M. Sigrist, "Time-reversal symmetry-breaking superconductivity in sr2ruo4", Nature **394**, 558–561 (1998), https://www.nature.com/articles/29038.

[14]S. K. Ghosh, M. Smidman, T. Shang, J. F. Annett, A. D. Hillier, J. Quintanilla, and H. Yuan, "Recent progress on superconductors with time-reversal symmetry breaking", **33**, 033001 (2020), https://doi.org/10.1088/1361-648x/abaa06.

[15]Z. F. Weng, J. L. Zhang, M. Smidman, T. Shang, J. Quintanilla, J. F. Annett, M. Nicklas, G. M. Pang, L. Jiao, W. B. Jiang, Y. Chen, F. Steglich, and H. Q. Yuan, "Two-gap superconductivity in $LaNiGa_2$ with nonunitary triplet pairing and even parity gap symmetry", Phys. Rev. Lett. **117**, 027001 (2016), https://link.aps.org/doi/10.1103/PhysRevLett.117.027001.

[16]C. M. Puetter and H.-Y. Kee, "Identifying spin-triplet pairing in spin-orbit coupled multi-band superconductors", **98**, 27010 (2012), https://doi.org/10.1209/0295-5075/98/27010.

[17]J. Linder and A. V. Balatsky, "Odd-frequency superconductivity", Rev. Mod. Phys. **91**, 045005 (2019), https://link.aps.org/doi/10.1103/RevModPhys.91.045005.

[18]D. F. Agterberg, P. M. R. Brydon, and C. Timm, "Bogoliubov fermi surfaces in superconductors with broken time-reversal symmetry", Phys. Rev. Lett. **118**, 127001 (2017), https://link.aps.org/doi/10.1103/PhysRevLett.118.127001.

[19]H. G. Suh, H. Menke, P. M. R. Brydon, C. Timm, A. Ramires, and D. F. Agterberg, "Stabilizing even-parity chiral superconductivity in Sr_2RuO_4", Phys. Rev. Research **2**, 032023 (2020), https://link.aps.org/doi/10.1103/PhysRevResearch.2.032023.

[20]A. M. Black-Schaffer and A. V. Balatsky, "Odd-frequency superconducting pairing in multiband superconductors", Physical Review B **88**, 104514 (2013), https://link.aps.org/doi/10.1103/PhysRevB.88.104514.

[21]S. Kanasugi and Y. Yanase, "Anapole superconductivity from $\mathcal{PT}$-symmetric mixed-parity interband pairing", arXiv:2107.07096 [cond-mat], arXiv: 2107.07096 (2021), http://arxiv.org/abs/2107.07096.

[22]S. Hüfner and T. Huber, *Photoelectron spectroscopy: principles and applications*, Advanced Texts in Physics (Springer, 2003), https://books.google.co.jp/books?id=WfOw6jP9-oIC.

[23]**光電子固体物性**, 現代物理学「展開シリーズ」(朝倉書店, 2011), https://books.google.co.jp/books?id=tc61uAAACAAJ.

[24]A. Damascelli, Z. Hussain, and Z.-X. Shen, “Angle-resolved photoemission studies of the cuprate superconductors”, Rev. Mod. Phys. **75**, 473–541 (2003), https://link.aps.org/doi/10.1103/RevModPhys.75.473.

[25]**強相関物質の基礎: 原子, 分子から固体へ**, 材料学シリーズ (内田老鶴圃, 2005), https://books.google.co.jp/books?id=0QdgPQAACAAJ.

[26]M. P. Seah and W. A. Dench, “Quantitative electron spectroscopy of surfaces: a standard data base for electron inelastic mean free paths in solids”, Surface and Interface Analysis **1**, 2–11 (1979), http://onlinelibrary.wiley.com/doi/10.1002/sia.740010103/abstract.

[27]K. Okazaki, Y. Ota, Y. Kotani, W. Malaeb, Y. Ishida, T. Shimojima, T. Kiss, S. Watanabe, C.-T. Chen, K. Kihou, C. H. Lee, A. Iyo, H. Eisaki, T. Saito, H. Fukazawa, Y. Kohori, K. Hashimoto, T. Shibauchi, Y. Matsuda, H. Ikeda, H. Miyahara, R. Arita, A. Chainani, and S. Shin, “Octet-line node structure of superconducting order parameter in kfe2as2”, Science **337**, 1314–1317 (2012), http://science.sciencemag.org/content/337/6100/1314.

[28]木須孝幸, 富樫格, S. Shin, and 渡部俊太郎, “レーザー励起光電子分光: 超高分解能とその応用”, 固体物理 **40**, 353–361 (2005), https://jglobal.jst.go.jp/detail?JGLOBAL_ID=200902205848894683.

[29]孝幸木須, 格富樫, 埴辛, and 俊太郎渡部, “レーザー励起超高分解能光電子分光”, 表面科学 **26**, 716–720 (2005).

[30]J. Sakuma, Y. Asakawa, and M. Obara, “Generation of 5-w deep-uv continuous-wave radiation at 266 nm by an external cavity with a cslib6o10 crystal”, Optics Letters **29**, 92–94 (2004), https://www.osapublishing.org/ol/abstract.cfm?uri=ol-29-1-92.

[31]M. Oka, N. Eguchi, L. Y. Liu, W. Wiechmann, and S. Kubota, “1-w cw 266-nm radiation from an external resonant cavity using a novel voice-coil- motor actuator”, in Conference on lasers and electro-optics (1994), paper cthm1 (May 1994), CThM1, https://www.osapublishing.org/abstract.cfm?uri=CLEO-1994-CThM1.

[32]R. W. P. Drever, J. L. Hall, F. V. Kowalski, J. Hough, G. M. Ford, A. J. Munley, and H. Ward, “Laser phase and frequency stabilization using an optical resonator”, Applied Physics B **31**, 97–105 (1983), https://doi.org/10.1007/BF00702605.

[33]T. Südmeyer, Y. Imai, H. Masuda, N. Eguchi, M. Saito, and S. Kubota, “Efficient 2nd and 4th harmonic generation of a single-frequency, continuous-wave fiber amplifier”, Optics Express **16**, 1546–1551 (2008), https://www.osapublishing.org/oe/abstract.cfm?uri=oe-16-3-1546.

[34]E. D. Black, “An introduction to pound–drever–hall laser frequency stabilization”, American Journal of Physics **69**, 79–87 (2000), https://aapt.scitation.org/doi/abs/10.1119/1.1286663.

[35]F.-C. Hsu, J.-Y. Luo, K.-W. Yeh, T.-K. Chen, T.-W. Huang, P. M. Wu, Y.-C. Lee, Y.-L. Huang, Y.-Y. Chu, D.-C. Yan, and M.-K. Wu, “Superconductivity in the pbo-type structure α-fese”, Proceedings of the National Academy of Sciences **105**, 14262–14264 (2008), https://www.pnas.org/content/105/38/14262.

[36]S. Medvedev, T. M. McQueen, I. A. Troyan, T. Palasyuk, M. I. Eremets, R. J. Cava, S. Naghavi, F. Casper, V. Ksenofontov, G. Wortmann, and C. Felser, "Electronic and magnetic phase diagram of $\beta-$fe1.01se with superconductivity at 36.7 k under pressure", Nature Materials **8**, 630–633 (2009), https://www.nature.com/articles/nmat2491.

[37]Q.-Y. Wang, Z. Li, W.-H. Zhang, Z.-C. Zhang, J.-S. Zhang, W. Li, H. Ding, Y.-B. Ou, P. Deng, K. Chang, J. Wen, C.-L. Song, K. He, J.-F. Jia, S.-H. Ji, Y.-Y. Wang, L.-L. Wang, X. Chen, X.-c. Ma, and Q.-K. Xxue, "Interface-induced high-temperature superconductivity in single unit-cell fese films on srtio 3", Chinese Physics Letters **29**, 037402 (2012), https://doi.org/10.1088/0256-307x/29/3/037402.

[38]T. M. McQueen, A. J. Williams, P. W. Stephens, J. Tao, Y. Zhu, V. Ksenofontov, F. Casper, C. Felser, and R. J. Cava, "Tetragonal-to-orthorhombic structural phase transition at 90 k in the superconductor $Fe_{1.01}Se$", Phys. Rev. Lett. **103**, 057002 (2009), https://link.aps.org/doi/10.1103/PhysRevLett.103.057002.

[39]R. M. Fernandes, A. V. Chubukov, and J. Schmalian, "What drives nematic order in iron-based superconductors?", Nature Physics **10**, 97–104 (2014), https://www.nature.com/articles/nphys2877.

[40]P. Dai, "Antiferromagnetic order and spin dynamics in iron-based superconductors", Rev. Mod. Phys. **87**, 855–896 (2015), https://link.aps.org/doi/10.1103/RevModPhys.87.855.

[41]T. Hashimoto, Y. Ota, H. Q. Yamamoto, Y. Suzuki, T. Shimojima, S. Watanabe, C. Chen, S. Kasahara, Y. Matsuda, T. Shibauchi, K. Okazaki, and S. Shin, "Superconducting gap anisotropy sensitive to nematic domains in fese", Nature Communications **9**, 282 (2018), https://www.nature.com/articles/s41467-017-02739-y.

[42]T. Shimojima, Y. Suzuki, T. Sonobe, A. Nakamura, M. Sakano, J. Omachi, K. Yoshioka, M. Kuwata-Gonokami, K. Ono, H. Kumigashira, A. E. Böhmer, F. Hardy, T. Wolf, C. Meingast, H. v. Löhneysen, H. Ikeda, and K. Ishizaka, "Lifting of xz/yz orbital degeneracy at the structural transition in detwinned fese", Phys. Rev. B **90**, 121111 (2014), https://link.aps.org/doi/10.1103/PhysRevB.90.121111.

[43]Y. Suzuki, T. Shimojima, T. Sonobe, A. Nakamura, M. Sakano, H. Tsuji, J. Omachi, K. Yoshioka, M. Kuwata-Gonokami, T. Watashige, R. Kobayashi, S. Kasahara, T. Shibauchi, Y. Matsuda, Y. Yamakawa, H. Kontani, and K. Ishizaka, "Momentum-dependent sign inversion of orbital order in superconducting fese", Phys. Rev. B **92**, 205117 (2015), https://link.aps.org/doi/10.1103/PhysRevB.92.205117.

[44]J. Maletz, V. B. Zabolotnyy, D. V. Evtushinsky, S. Thirupathaiah, A. U. B. Wolter, L. Harnagea, A. N. Yaresko, A. N. Vasiliev, D. A. Chareev, A. E. Böhmer, F. Hardy, T. Wolf, C. Meingast, E. D. L. Rienks, B. Büchner, and S. V. Borisenko, "Unusual band renormalization in the simplest iron-based superconductor $FeSe_{1-x}$", Phys. Rev. B **89**, 220506 (2014), https://link.aps.org/doi/10.1103/PhysRevB.89.220506.

[45]M. D. Watson, T. K. Kim, A. A. Haghighirad, N. R. Davies, A. McCollam, A. Narayanan, S. F. Blake, Y. L. Chen, S. Ghannadzadeh, A. J. Schofield, M. Hoesch, C. Meingast, T. Wolf, and A. I. Coldea, "Emergence of the nematic electronic state in fese", Phys. Rev. B **91**, 155106 (2015), https://link.aps.org/doi/10.1103/PhysRevB.91.155106.

[46]T. Watashige, Y. Tsutsumi, T. Hanaguri, Y. Kohsaka, S. Kasahara, A. Furusaki, M. Sigrist, C. Meingast, T. Wolf, H. v. Löhneysen, T. Shibauchi, and Y. Matsuda, "Evidence for time-reversal symmetry breaking of the superconducting state near twin-boundary interfaces in fese revealed by scanning tunneling spectroscopy", Phys. Rev. X **5**, 031022 (2015), https://link.aps.org/doi/10.1103/PhysRevX.5.031022.

[47]D. Liu, C. Li, J. Huang, B. Lei, L. Wang, X. Wu, B. Shen, Q. Gao, Y. Zhang, X. Liu, Y. Hu, Y. Xu, A. Liang, J. Liu, P. Ai, L. Zhao, S. He, L. Yu, G. Liu, Y. Mao, X. Dong, X. Jia, F. Zhang, S. Zhang, F. Yang, Z. Wang, Q. Peng, Y. Shi, J. Hu, T. Xiang, X. Chen, Z. Xu, C. Chen, and X. J. Zhou, "Orbital origin of extremely anisotropic superconducting gap in nematic phase of fese superconductor", Phys. Rev. X **8**, 031033 (2018), https://link.aps.org/doi/10.1103/PhysRevX.8.031033.

[48]T. Kuwayama, K. Matsuura, J. Gouchi, Y. Yamakawa, Y. Mizukami, S. Kasahara, Y. Matsuda, T. Shibauchi, H. Kontani, Y. Uwatoko, and N. Fujiwara, "Pressure-induced reconstitution of fermi surfaces and spin fluctuations in s-substituted fese", Scientific Reports **11**, 17265 (2021), https://www.nature.com/articles/s41598-021-96277-9.

[49]S. Hosoi, K. Matsuura, K. Ishida, H. Wang, Y. Mizukami, T. Watashige, S. Kasahara, Y. Matsuda, and T. Shibauchi, "Nematic quantum critical point without magnetism in fese1−xsx superconductors", Proceedings of the National Academy of Sciences **113**, 8139–8143 (2016), https://www.pnas.org/content/113/29/8139.

[50]J.-H. Chu, H.-H. Kuo, J. G. Analytis, and I. R. Fisher, "Divergent nematic susceptibility in an iron arsenide superconductor", Science **337**, 710–712 (2012), https://www.science.org/doi/abs/10.1126/science.1221713.

[51]Y. Sato, S. Kasahara, T. Taniguchi, X. Xing, Y. Kasahara, Y. Tokiwa, Y. Yamakawa, H. Kontani, T. Shibauchi, and Y. Matsuda, "Abrupt change of the superconducting gap structure at the nematic critical point in fese1−xsx", Proceedings of the National Academy of Sciences **115**, 1227–1231 (2018), https://www.pnas.org/content/115/6/1227.

[52]T. Hanaguri, K. Iwaya, Y. Kohsaka, T. Machida, T. Watashige, S. Kasahara, T. Shibauchi, and Y. Matsuda, "Two distinct superconducting pairing states divided by the nematic end point in fese1−xsx", Science Advances **4**, eaar6419 (2018), https://advances.sciencemag.org/content/4/5/eaar6419.

[53]M. Randeria and E. Taylor, "Crossover from bardeen-cooper-schrieffer to bose-einstein condensation and the unitary fermi gas", Annual Review of Condensed Matter Physics **5**, 209–232 (2014), https://doi.org/10.1146/annurev-conmatphys-031113-133829.

[54]C. A. Regal, M. Greiner, and D. S. Jin, "Observation of resonance condensation of fermionic atom pairs", Phys. Rev. Lett. **92**, 040403 (2004), https://link.aps.org/doi/10.1103/PhysRevLett.92.040403.

[55]T. Hashimoto, Y. Ota, A. Tsuzuki, T. Nagashima, A. Fukushima, S. Kasahara, Y. Matsuda, K. Matsuura, Y. Mizukami, T. Shibauchi, S. Shin, and K. Okazaki, "Bose-einstein condensation superconductivity induced by disappearance of the nematic state", Science Advances **6**, eabb9052 (2020), https://advances.sciencemag.org/content/6/45/eabb9052.

[56]Y. Mizukami, M. Haze, O. Tanaka, K. Matsuura, D. Sano, J. Böker, I. Eremin, S. Kasahara, Y. Matsuda, and T. Shibauchi, *Thermodynamics of transition to bcs-bec crossover superconductivity in fese*$_{1-x}$*s*$_x$, 2021.

[57]T. Shibauchi, T. Hanaguri, and Y. Matsuda, "Exotic superconducting states in fese-based materials", Journal of the Physical Society of Japan **89**, 102002 (2020), https://doi.org/10.7566/JPSJ.89.102002.

[58]K. Matsuura, M. Qiu, Q. Sheng, Y. P. Cai, K. Yamakawa, Z. Gugunchia, R. P. Day, K. M. Kojima, A. Damascelli, Y. Sugimura, M. Saito, T. Takenaka, K. Ishihara, Y. Mizukami, Y. Hashimoto K. andGu, S. L. Guo, L. C. Fu, Z. Zhang, F. L. Ning, G. Q. Zhao, G. Y. Dai, C. Q. Jin, J. W. Beare, G. M. Luke, Y. J. Uemura, and T. Shibauchi, "Transition from chiral nematic to ultranodal superconducting state in fese1−xsx", 2021.

[59]P. M. R. Brydon, D. F. Agterberg, H. Menke, and C. Timm, "Bogoliubov fermi surfaces: general theory, magnetic order, and topology", Phys. Rev. B **98**, 224509 (2018), https://link.aps.org/doi/10.1103/PhysRevB.98.224509.

[60]C. J. Lapp, G. Börner, and C. Timm, "Experimental consequences of bogoliubov fermi surfaces", Phys. Rev. B **101**, 024505 (2020), https://link.aps.org/doi/10.1103/PhysRevB.101.024505.

[61]C. Setty, Y. Cao, A. Kreisel, S. Bhattacharyya, and P. J. Hirschfeld, "Bogoliubov fermi surfaces in spin-$\frac{1}{2}$ systems: model hamiltonians and experimental consequences", Phys. Rev. B **102**, 064504 (2020), https://link.aps.org/doi/10.1103/PhysRevB.102.064504.

[62]C. Setty, S. Bhattacharyya, Y. Cao, A. Kreisel, and P. J. Hirschfeld, "Topological ultranodal pair states in iron-based superconductors", Nature Communications **11**, 523 (2020), https://www.nature.com/articles/s41467-020-14357-2.

[63]A. E. Böhmer, F. Hardy, F. Eilers, D. Ernst, P. Adelmann, P. Schweiss, T. Wolf, and C. Meingast, "Lack of coupling between superconductivity and orthorhombic distortion in stoichiometric single-crystalline fese", Phys. Rev. B **87**, 180505 (2013), https://link.aps.org/doi/10.1103/PhysRevB.87.180505.

[64]P. Zhang, K. Yaji, T. Hashimoto, Y. Ota, T. Kondo, K. Okazaki, Z. Wang, J. Wen, G. D. Gu, H. Ding, and S. Shik, "Observation of topological superconductivity on the surface of an iron-based superconductor", Science **360**, 182–186 (2018), https://www.science.org/doi/10.1126/science.aan4596.

[65]A. I. Coldea, S. F. Blake, S. Kasahara, A. A. Haghighirad, M. D. Watson, W. Knafo, E. S. Choi, A. McCollam, P. Reiss, T. Yamashita, M. Bruma, S. C. Speller, Y. Matsuda, T. Wolf, T. Shibauchi, and A. J. Schofield, "Evolution of the low-temperature fermi surface of superconducting fese1−xsx across a nematic phase transition", npj Quantum Materials **4**, 1–7 (2019), https://www.nature.com/articles/s41535-018-0141-0.

[66]大田由一, **極低温超高分解能レーザー光電子分光の開発と鉄系超伝導体** *ba1-xkxfe2as2* **の研究**, PhD thesis (2014).

[67]Y. Cao, J. A. Waugh, X. W. Zhang, J.-W. Luo, Q. Wang, T. J. Reber, S. K. Mo, Z. Xu, A. Yang, and J. Schneeloch, "Mapping the orbital wavefunction of the surface states in three-dimensional topological insulators", Nature Physics **9**, 499 (2013).

[68]Y. Hirose, T. Kishino, J. Sakaguchi, Y. Miura, F. Honda, T. Takeuchi, E. Yamamoto, Y. Haga, H. Harima, R. Settai, and Y. Ōnuki, "Fermi surface and superconducting properties of non-centrosymmetric lanic2", Journal of the Physical Society of Japan **81**, 113703 (2012), https://doi.org/10.1143/JPSJ.81.113703.

[69]S. Yonezawa, K. Tajiri, S. Nakata, Y. Nagai, Z. Wang, K. Segawa, Y. Ando, and Y. Maeno, "Thermodynamic evidence for nematic superconductivity in cu x bi 2 se 3", Nature Physics **13**, 123–126 (2017), https://www.nature.com/articles/nphys3907.

[70]L. Fu, "Odd-parity topological superconductor with nematic order: application to $Cu_xBi_2Se_3$", Phys. Rev. B **90**, 100509 (2014), https://link.aps.org/doi/10.1103/PhysRevB.90.100509.

[71]Y. Yamakawa, S. Onari, and H. Kontani, "Nematicity and magnetism in fese and other families of fe-based superconductors", Phys. Rev. X **6**, 021032 (2016), https://link.aps.org/doi/10.1103/PhysRevX.6.021032.

[72]M. Qiu, K. Matsuura, T. Takenaka, Y. Sugimura, T. Shibauchi, Q. Sheng, K. Yamakawa, J. Y. Uemura, Y. Cai, A. Damascelli, P. R. Day, K. Kojima, W. J. Beare, G. Luke, G. Z. Qiang, C. Jin, Y. Gu, C. L. Fu, F. Ning, and M. Saito, "Aps -aps march meeting 2020 - event - time-reversal symmetry-breaking superconductivity in fese1-xsx", in Bulletin of the american physical society, Vol. Volume 65, Number 1 (), https://meetings.aps.org/Meeting/MAR20/Session/J61.4.

Acknowledgement

I would like to express my gratitude to my supervisor Prof. Kozo Okazaki for guiding me ahead toward this way and providing the best environment to research. Also I would like to show my appreciate to Prof. Shik Shin for giving me advice about research and development of the new light source.

I would like to thank to Dr. Yuichi Ota, Dr. Takahiro Hashimoto and Mr. Akihiro Tsuzuki for imparting knowledge and skill to manage and make the best use of the precise laser ARPES system. I would like to thank to Prof. Takeshi Kondo and Prof. Toshiyuki Taniuchi for giving me incisive comments about machine, data and experiments. I would like to thank Dr. Takeshi Suzuki for providing Bi_2Se_3 samples and giving advice about experiments and construction of optics. I would like to thank to Dr.Kenta Kuroda also for providing other Bi_2Se_3 samples. I would like to thank to Dr. Yukiaki Ishida for providing counsel about ARPES with low excitation energy. I would like to thank to Dr. Shunsuke Sakuragi, Dr. Peng Zhang, for teaching knowledge

I am grateful to Prof. Takasada Shibauchi, Prof. Kenichiro Hashimoto, Dr. Yuta Mizukami and Dr. Kohei Matsuura for providing high-quality single crystal samples of $FeSe_{1-x}S_x$ and fruitful discussion. I am grateful to Dr. Hiroaki Nakao who gave advice and help a lot in the collaboration for the development of the new light source. I am grateful to Dr. Masami Fujisawa for consultations to design the new chamber for switching the light sources. I am grateful to Dr. Yusuke Hirose for supplying $LaNiC_2$ samples.

I am indebted to members of Prof. Okazaki, Prof. Shin and Prof. Kondo groups for constant support and encouragement. I would like to express my appreciation to Mr. Sahand Najafzadeh, Mr. Shunichiro, Mr. Akifumi Mine Dr. Weilu Zhang, Mrs. Akiko Fukushima and Dr. Yigui Zhong for help and support of managements of the machine. I would like to thank to Dr. Cédric Bareille, Dr. Masaya Takeuchi, Dr. Hirokazu Fujiwara, Dr. Mitsuhiro Yamamoto, Dr. Haruyoshi Motoyui, Dr. Shuntaro Akebi, Dr. Ryo Noguchi, Dr. So Kunisada, Fr. Chun Lin. Dr. Quianhui Ren, Dr. Kaishu Kawaguchi, Dr. Yuxuan Wan, Mr. Shoya Michimae, Mr. Junpei Kawakita, Mr. Daiki Matsumaru, Mr. Mari Watanabe, Mr. Xu Jiadi, Mr. Kihu Kurokawa, Mr. Yosuke Arai, Mr. Yuji Okuda, Mr. Yuya Mizoguchi, Mr. Hiroaki Tanaka, Mr. Yuki Akimoto, Mr.Kecheng Liu, Mr. Youichi Kageyama, Mr. Yuyang Dong, Mr. Kohei Aido, Kei Kato, Yuto Fukushima for encouragement.

I would like to express my gratitude to Mrs. Sachiko Shinei, Mrs. Akiko Fukushima and Mrs. Yui, Mizuno for their great help paperwork and a variety of consultations.

I acknowledge financial supports from the "Fostering Advanced Human Resources to Lead Green Transformation (GX)" project of Support for Pioneering Research Initiated by Next Generation (SPRING) of Japan Science and Technology Agency (JST).

I would thank to my parents and brother for encouragement and financial support. I also thank to myself who have survived through this path.

I am full of gratitude to all of which this life of the study consists.

和文抄訳

論文の内容の要旨

論文題目 Study of novel superconducting states in tetragonal phase of Fe(Se, S) by laser-based angle-resolved photoemission spectroscopy
（レーザー角度分解光電子分光による正方晶相 Fe(Se, S) における超伝導状態の研究）

氏名 長島 椿

1. 序論

1911 年に発見された超伝導は、完全導電性やマイスナー効果等の特徴や巨視的量子現象であるという観点から、基礎と応用の両面で興味深い現象である。超伝導体には大別して、BCS 理論に従ってフォノンを媒介したクーパー対を形成する従来型と、BCS 理論で説明できない非従来型がある。後者については多様な新奇物性が報告される一方で、一般にその転移温度（T_c）は低く、超伝導体状態を特徴付ける超伝導ギャップも小さいため、実験による調査は困難である。我々は低い T_c を有する超伝導体のギャップ構造を明らかにするべく、高強度連続波レーザーを用いて低温高分解能レーザー角度分解光電子分光（ARPES）測定の実現を目指した。また非従来型超伝導の中でも、従来受け入れられてきたギャップ構造の区分を覆し近年注目される、ボゴリューボフフェルミ面（BFS）の存在を研究対象とし測定を行った [12]。

2. 測定装置

ARPES は電子構造を直接観測できる強力な測定手法であり、超伝導ギャップ構造を調べる上でも非常に有用である。本研究で用いられた装置は、アナライザーに Scienta Omicron HR8000、励起光源に 7 eV 疑似連続波レーザー（繰り返し周波数 960 MHz）を用いており、最低温 1 K、最高分解能 70 μeV という記録的な性能を有するが [2]、最高分解能での測定は効率の観点から実用的ではなかった。本問題の解

決のため、分解能向上を妨げる空間電荷効果を回避する程の低ピーク強度且つ、高測定効率を実現する高平均強度を持つ光源の導入が必要だった。

3. 新規光源導入

高分解能 ARPES 測定のための新規光源として、深紫外高強度連続波レーザーを株式会社オキサイドと合同で開発・導入した。最終的な性能は、従来光源と比較しつつ表 1 にまとめた。基本波には 852 nm の外部共振器ダイオードレーザーを用いており、2 段階の第二次高調波発生をそれぞれ非線形光学結晶 LBO と β-BBO を用いて行い、213 nm（5.8 eV）を出力している。
導入直後では 213 nm 光の発振自体が不安定だったが、振動への対策や電源の安定化、種光の交換、BBO 結晶の交換と Ar フローの導入等の改良を経て、最高分解能測定の実用化を果たした。一方で高分解能測定時に用いるアナライザーの幅狭なスリットは、工作精度の問題で端面が歪な構造を有し、光電子の軌道に影響を与え最終的に得られるイメージを歪ませてしまうことがある。実際に本測定系においても最高分解能設定を含み幾つかのスリット使用時に E-k プロットに線状の構造が現れる。そこで比較的幅の狭いスリットを使用することで、125 μeV という高エネルギー分解能を維持しつつ明瞭なバンド分散の観測が可能となり、更にスリットを拡げたことにより確保できた余剰の光強度を活かしエキスパンダー光学を導入しスポット径を $\sim$ 80 μm まで縮小したことにより、空間分解能も向上した。

Table 1.: 従来光源と新規光源の最終的な性能の比較

励起エネルギー	発振動作	強度	スポット径	結晶雰囲気
5.8 eV	CW	$\sim$ 1 mW	$\sim$ 80 μm	Ar
7 eV	q-CW ($\leq$ 960 MHz)	$\sim$ 10 μW	$\sim$ 150 μm	N_2

4. $FeSe_{1-x}S_x$ における新奇なウルトラノーダル状態

4.1 背景

超伝導ギャップ構造は一般に、ノードを持たないフルギャップ・波数空間で点状にノードをもつポイントノード・線上にノードをもつラインノードの 3 種に大別され議論が行われてきた。しかし近年、マルチバンド系の超伝導体において、新たにボゴリューボフフェルミ面と呼ばれる面状のノードを有するウルトラノーダル状態の実現が予想され、幾つかの物質がそのプラットフォームとして候補に挙がっており、その一つが $FeSe_{1-x}S_x$ である [3]。
母物質の鉄系超伝導体 FeSe（$T_c = 9$ K）は、Fe 原子と Se 原子が交互に並ぶレイヤー

から成る層状物質であり、鉄系超伝導体の中でも最も単純な結晶構造をもつ [4]。また単原子層試料や高圧下で 50 K 以上へ転移温度の上昇が報告されたことから、高温超伝導体の候補としても期待される [5]。更に T_s ~90 K を境に、正方晶から斜方晶への構造相転移に伴いネマティック相へ転移し、その影響が超伝導状態の異方性に表れる [6]。

Se サイトを等原子価の S で置換した $FeSe_{1-x}S_x$ 系では、$x = 0.17$ においてネマティック相が消失して正方晶相へ転移し、またその近傍でネマティック感受率が発散することから、本組成はネマティック量子臨界点（NQP）と考えられている [7]。正方晶相では、ネマティック相とは異なる超伝導状態の実現を示す結果が報告されており、特に残留状態密度が NQP を境に増加する振る舞いが確認されている [8, 9]。これらの実験結果が不純物による影響でないことは、試料について量子振動測定が行われた事や STM 測定の結果から確認されている [9]。

本研究ではレーザー ARPES を用いて、単結晶 $FeSe_{0.78}S_{0.22}$（T_c ~4 K）のブリルアンゾーン中央に存在するホールバンドにおける超伝導ギャップについて調べた。試料は化学蒸気輸送法を用いて作製され [10]、試料清浄表面は超高真空下（~10-8 Pa）で劈開して得られた。

4.2 測定結果

本項の内容は、投稿論文の形で刊行される予定であるため、学位授与日から 5 年間インターネットでの公表をすることができません。

参考文献

[1] D. F. Agterberg, *et al.*, Phys. Rev. Lett. **118**, 127001 (2017).

[2] Okazaki, K. *et al.*, Science **337**, 1314 – 1317 (2012).

[3] C. Setty, *et al.*, Nat. Commun. **11**, 523 (2020).

[4] F.-C. Hsu *et al.*, PNAS. **105**, 14262 – 14264 (2008).

[5] Q.-Y. Wang *et al.*, Chin. Phys. Lett. **29**, 037402 (2012).

[6] T. M. McQueen, *et al.*, Phys. Rev. Lett. **103**, 057002 (2009).

[7] S. Hosoi *et al.*, PNAS. **113**, 8139 – 8143 (2016).

[8] Y. Sato *et al.*, PNAS. **115**, 1227 – 1231 (2018).

[9] T. Hanaguri *et al.*, Sci. Adv. **4**, eaar6419 (2018).

[10] A. E. Böhmer *et al.*, Phys. Rev. B. **87**, 180505 (2013).

[11] T. Hashimoto *et al.*, Nat. Commun. **9**, 282 (2018).

[12] A. I. Coldea *et al.*, npj Quant. Mater. **4**, 1 – 7 (2019).

[13] C. Setty, S. Bhattacharyya, Y. Cao, A. Kreisel, P. J. Hirschfeld, Nat. Commun. **11**, 523 (2020).

[14] K. Matsuura, *et al.*, *unpublished.*